



ELSEVIER

Comput. Methods Appl. Mech. Engrg. 139 (1996) 195–227

**Computer methods
in applied
mechanics and
engineering**

Reproducing Kernel Particle Methods for large deformation analysis of non-linear structures

Jiun-Shyan Chen^{*,1}, Chunhui Pan², Cheng-Tang Wu², Wing Kam Liu³

*The University of Iowa, Department of Mechanical Engineering & Center for Computer-Aided Design,
2133 Engineering Building, Iowa City, IA 52242-1527, USA*

Received 24 April 1996

Abstract

Large deformation analysis of non-linear elastic and inelastic structures based on Reproducing Kernel Particle Methods (RKPM) is presented. The method requires no explicit mesh in computation and therefore avoids mesh distortion difficulties in large deformation analysis. The current formulation considers hyperelastic and elasto-plastic materials since they represent path-independent and path-dependent material behaviors, respectively. In this paper, a material kernel function and an RKPM material shape function are introduced for large deformation analysis. The support of the RKPM material shape function covers the same set of particles during material deformation and hence no tension instability is encountered in the large deformation computation. The essential boundary conditions are introduced by the use of a transformation method. The transformation matrix is formed only once at the initial stage if the RKPM material shape functions are employed. The appropriate integration procedures for the moment matrix and its derivative are studied from the standpoint of reproducing conditions. In transient problems with an explicit time integration method, the lumped mass matrices are constructed at nodal coordinate so that masses are lumped at the particles. Several hyperelasticity and elasto-plasticity problems are studied to demonstrate the effectiveness of the method. The numerical results indicated that RKPM handles large material distortion more effectively than finite elements due to its smoother shape functions and, consequently, provides a higher solution accuracy under large deformation. Unlike the conventional finite element approach, the nodal spacing irregularity in RKPM does not lead to irregular mesh shape that significantly deteriorates solution accuracy. No volumetric locking is observed when applying non-linear RKPM to nearly incompressible hyperelasticity and perfect plasticity problems. Further, model adaptivity in RKPM can be accomplished simply by adding more points in the highly deformed areas without remeshing.

1. Introduction

In computational mechanics, the finite element formulations dealing with geometric and material non-linearities have been well developed and a significant amount of work has been accomplished in large deformation analysis. Nevertheless, standard finite element approaches are still ineffective in handling extreme material distortions owing to severe mesh distortion. Some finite element methods such as the Arbitrary Lagrangian Eulerian (ALE) method [1,2] have been introduced to allow continuous remeshing during computation; however, the convective effect needs to be appropriately treated to avoid oscillation and thus requires additional efforts.

A class of meshless methods have been developed, including Smooth Particle Hydrodynamics (SPH)

* Corresponding author.

¹ Assistant Professor, The University of Iowa, Department of Mechanical Engineering and Center for Computer Aided Design.

² Research Assistant, The University of Iowa, Department of Mechanical Engineering and Center for Computer Aided Design.

³ Professor, Northwestern University, Department of Mechanical Engineering, 2145 Sheridan Road, Evanston, IL 60208.

[3–7], Particle in Cell Methods (PIC) [8–10], Diffuse Element Methods (DEM) [11], Element Free Galerkin Methods (EFG) [12–16] and Reproducing Kernel Particle Methods (RKPM) [17–24]. The advantages and disadvantages of these methods have been discussed and compared in Belytschko et al. [14,16], Liu et al. [17,18,22], and in non-linear elastic problems by Chen et al. [24]. In general, these methods share the same characteristic: the domain of interest is completely discretized by nodes, and this unique characteristic motivates the development of this work.

Among the meshless methods, EFG and RKPM have been demonstrated as most suitable for structural analysis. The foundation of EFG proposed by Belytschko et al. [12–16] is the moving least-squares method originally proposed by Lancaster et al. [25], and was first applied to computational mechanics under the name DEM by Nayroles et al. [11]. Several drawbacks in DEM were corrected in EFG to enhance accuracy. For example, a large number of quadrature points were used in EFG to provide better solution accuracy. Certain terms in the derivatives of the interpolants which were omitted in DEM were included in EFG and were shown to improve solution accuracy. EFG also enforces the essential boundary conditions by a Lagrange multiplier method. The numerical studies reported in [12,13] suggest that EFG does not exhibit volumetric locking, and the rate of convergence for the method is significantly higher than that of finite elements. The studies also demonstrated that EFG is very effective in fracture problems that are difficult to handle using finite elements. The efficiency of EFG was later improved through the use of a modified variational principle to enforce essential boundary conditions [13], and the derivative of shape function was calculated by a faster derivative method [16].

Liu et al. [17–23] took a different approach to introduce a Reproducing Kernel Particle Method. They introduced a correction function in the kernel of integral transformation to impose reproducing conditions. Adding the correction function in the kernel significantly enhances the solution accuracy when compared to that of SPH. The method of using integral transformation with a corrected kernel function is called the Reproducing Kernel Particle Method, since it satisfies the reproduction conditions and therefore exactly reproduces polynomials. This method provides a general formulation for the construction of shape functions for meshless computation. Using specific discretization of the reproducing equation, EFG and SPH methods can be recovered. Liu et al. [18–20,22] also combined the theory of wavelet analysis in RKPM by introducing the scaling function as the kernel function and successfully applied RKPM to multiple scale analysis. The convergence properties of RKPM and the moving least-squares reproducing kernel particle methods are discussed in [22] and [21], respectively. To the author's knowledge, this is the first presentation of a rigorous mathematical formulation for meshless methods. Chen et al. [24] later further extend RKPM to non-linear elasticity.

This paper presents the implementation of the Reproducing Kernel Particle Method, with additional studies and developments, for the large deformation analysis of non-linear structures. The application to both path-independent and path-dependent materials with emphasis on hyperelasticity and elastoplasticity, is discussed. Since the RKPM shape functions are obtained by the discretization of a reproducing equation that satisfies the reproducing conditions in a continuum form, it is important to examine the appropriate integration method for the moment matrix and its derivatives so that the reproducing conditions are still retained after discretization. As discussed by Liu et al. [17,18,22], in RKPM computation the support of the kernel function must cover enough particles for the method to be stable. The necessary conditions for kernel stability and for the correction function stability are given in [17,18] and [21], respectively. Using the kernel function with a fixed support size could lead to instability when materials undergo large deformation. Continuous re-adjustment of kernel function support size could circumvent this difficulty but creates an additional burden. In this work, we introduce a material kernel function that deforms with the material. The support of the material kernel function covers the same set of particles throughout the course of deformation and therefore avoids instability in large deformation analysis.

Because the meshless shape functions do not pass through the data, the essential boundary conditions cannot be imposed by the method used in finite element approach. The early work by Nayroles et al. [11] used a low-order quadrature rule that did not impose essential boundary conditions exactly. Belytschko et al. [12] employed a Lagrange multiplier method to enforce essential boundary conditions, and this method passed a linear patch test. However, additional Lagrange multipliers need to be solved

and the method is particularly ineffective in non-linear problems since more unknowns are to be solved at every incremental step. The efficiency of the method was later improved by Lu et al. [13] to replace the Lagrange multiplier by a surface traction which is an energy-conjugate variable of the prescribed displacements. Nevertheless, for non-linear problems, the involvement of constitutive equations in this approach complicates the numerical procedures, especially for path-dependent materials or incompressible materials. In this work, we propose to use a method that transforms the generalized displacements to nodal displacements. With this transformation, a modified shape function that possesses Kronecker delta properties can be developed, and the point load can be directly applied. This method exactly imposes the essential boundary conditions; hence, no error is accumulated during non-linear iteration. Admittedly, additional effort is needed to form the transformation matrix and its inverse. Yet, for non-linear problems the transformation matrix and its inverse are performed only once at the initial stage if the RKPM shape function is constructed in the material coordinate and therefore the additional effort is justifiable.

This paper is organized as follows: In Section 2, the development of RKPM shape function is described. The appropriate integration method for moment matrix and its derivative to retain the reproducing conditions in the discrete reproducing equation is discussed. Section 3 presents the implementation of RKPM for large deformation analyses. In this section, the material kernel function and material shape function are introduced, and the transformation method to directly impose essential boundary conditions is discussed. In Section 4, numerical procedures for RKPM large deformation analysis is given. Construction of lumped mass matrix in the nodal coordinate is presented in Section 5. Numerical results are presented in Section 6 to demonstrate the effectiveness of this implementation, and followed by conclusions and discussions in Section 7.

2. Review of Reproducing Kernel Particle Methods

2.1. Reproducing kernel shape functions

We begin with the integral transformation of a function $u(x)$ by

$$v(x) = Tu = \int_{\Omega} \Phi(x, s)u(s) ds \quad (2.1)$$

where $\Phi(x, s)$ is known as the kernel of the transformation. The transformation T is linear since $T(u_1 + u_2) = Tu_1 + Tu_2$ and $T(\alpha u) = \alpha Tu$. If the kernel $\Phi(x, s)$ is chosen to be close to $\delta(x - s)$, then $v(x) \rightarrow u(x)$. Therefore, Eq. (2.1) is often referred to as the kernel estimation of the function $u(x)$. In SPH, the kernels with small compact support are usually selected so that Eq. (2.1) approximates $u(x)$. However, it is first observed by Liu et al. [18] that when Eq. (2.1) is applied to discretized finite domains in SPH applications, the numerical solutions exhibit amplitude and phase errors in addition to solution deterioration near the boundaries. Liu et al. [17–19] explained this phenomenon by the failure to meet the completeness requirement and introduced the following reproducing equation

$$u^a(x) = \int_{\Omega} \bar{\Phi}_a(x; x - s)u(s) ds \quad (2.2)$$

where $u^a(x)$ is called the reproduced function of $u(x)$, and $\bar{\Phi}_a(x; x - s)$ is the modified kernel function that is expressed by

$$\bar{\Phi}_a(x; x - s) = C(x; x - s)\Phi_a(x - s) \quad (2.3)$$

$$\Phi_a(x - s) = \frac{1}{a} \Phi\left(\frac{x - s}{a}\right) \quad (2.4)$$

where a is the dilation parameter of the kernel function $\Phi_a(x - s)$ and $C(x; x - s)$ is called the correction function which is obtained by imposing the reproducing conditions such that the reproducing equation

(Eq. (2.2)) exactly reproduces polynomials. The correction function $C(x; x-s)$ proposed by Liu et al. [17,18,22] is expressed by a linear combination of polynomial basis functions in the following form:

$$C(x; x-s) = \sum_{i=0}^N b_i(x)(x-s)^i \equiv \mathbf{H}^T(x-s)\mathbf{b}(x) \quad (2.5)$$

where

$$\mathbf{H}^T(x-s) = [1, x-s, (x-s)^2, \dots, (x-s)^N] \quad (2.6)$$

$$\mathbf{b}^T(x) = [b_0(x), b_1(x), \dots, b_N(x)] \quad (2.7)$$

\mathbf{H} is a vector of basis functions and $b_i(x)$'s are functions of x which are to be determined. Consider the following Taylor series expansion of $u(x)$:

$$u(s) = \sum_{n=0}^{\infty} \frac{(s-x)^n}{n!} u^{(n)}(x) \quad (2.8)$$

where $u^{(n)} = d^n u / dx^n$. Substituting Eq. (2.8) into Eq. (2.2) leads to

$$u^a(x) = \bar{m}_0(x)u(x) + \sum_{n=1}^{\infty} \frac{(-1)^n}{n!} \bar{m}_n(x)u^{(n)}(x) \quad (2.9)$$

where

$$\bar{m}_n(x) = \int_{\Omega} (x-s)^n \bar{\Phi}_a(x-s) ds = \sum_{k=0}^N b_k(x) \tilde{m}_{n+k}(x) \quad (2.10)$$

and

$$\tilde{m}_n(x) = \int_{\Omega} (x-s)^n \Phi_a(x-s) ds \quad (2.11)$$

To satisfy the N th order completeness requirement, i.e. for Eq. (2.9) to exactly reproduce N th order polynomials, the following conditions need to be satisfied

$$\bar{m}_0(x) = 1 \quad (2.12)$$

and

$$\bar{m}_i(x) = 0 \quad \text{for } i = 1, \dots, N \quad (2.13)$$

Eqs. (2.12) and (2.13) represent the following set of equations

$$\tilde{\mathbf{M}}(x)\mathbf{b}(x) = \mathbf{H}(0) \quad (2.14)$$

where $\tilde{\mathbf{M}}(x)$ is the moment matrix defined by

$$\tilde{\mathbf{M}}(x) = \int_{\Omega} \mathbf{H}(x-s)\mathbf{H}^T(x-s)\Phi_a(x-s) ds \quad (2.15)$$

Solving $\mathbf{b}(x)$ from Eq. (2.14), the correction function is obtained:

$$C(x; x-s) = \mathbf{H}^T(0)\tilde{\mathbf{M}}^{-1}(x)\mathbf{H}(x-s) \quad (2.16)$$

It is apparent that $\tilde{\mathbf{M}}$ is the Gram matrix of a set of basis functions $\{1, x-s, (x-s)^2, \dots, (x-s)^N\}$ with respect to Φ_a . It is known that this set of basis functions is linearly independent in the sense of the scalar product (\cdot, \cdot) . Further, it is also known that if a set of basis functions is linearly independent in the sense of (\cdot, \cdot) , and if Φ_a is a positive or negative function, then this set of basis functions is also linearly independent with respect to Φ_a , in the sense of $(\cdot, \cdot)_{\Phi}$. Since Φ_a is chosen to be a positive function, and

$\{1, x-s, (x-s)^2, \dots, (x-s)^N\}$ are linearly independent with respect to Φ_a , therefore the Gram matrix $\tilde{\mathbf{M}}$ is non-singular.

The discretized reproducing equation is obtained by performing numerical integration in Eq. (2.2). An example of discretization is to employ the trapezoidal rule to the reproducing equation to yield

$$u^a(x) \cong \sum_{I=1}^{NP} \bar{\Phi}_a(x; x-x_I) u(x_I) \Delta x_I \equiv \sum_{I=1}^{NP} \Psi_I(x) u_I \quad (2.17)$$

and

$$\Psi_I(x) = \bar{\Phi}_a(x; x-x_I) \Delta x_I = \mathbf{H}^T(0) \tilde{\mathbf{M}}^{-1}(x) \mathbf{H}(x-x_I) \Phi_a(x-x_I) \Delta x_I \quad (2.18)$$

where NP is the total number of particles, and $\Psi_I(x)$'s can be interpreted as the shape functions of $u^R(x)$. Consequently, the derivative of $\Psi_I(x)$ is

$$\begin{aligned} \Psi_{I,x}(x) = & \mathbf{H}^T(0) [\tilde{\mathbf{M}}_{,x}^{-1}(x) \mathbf{H}(x-x_I) \Phi_a(x-x_I) + \tilde{\mathbf{M}}^{-1}(x) \mathbf{H}_{,x}(x-x_I) \Phi_a(x-x_I) \\ & + \tilde{\mathbf{M}}^{-1}(x) \mathbf{H}(x-x_I) \Phi_{a,x}(x-x_I)] \Delta x_I \end{aligned} \quad (2.19)$$

In this paper, we employ the cubic spline function as the kernel function:

$$\Phi(z_I) = \begin{cases} \frac{2}{3} - 4z_I^2 + 4z_I^3 & \text{for } 0 \leq |z_I| \leq \frac{1}{2} \\ \frac{4}{3} - 4z_I + 4z_I^2 - \frac{4}{3} z_I^3 & \text{for } \frac{1}{2} \leq |z_I| \leq 1 \\ 0 & \text{otherwise} \end{cases} \quad (2.20)$$

$$z_I = \frac{(x-x_I)}{a} \quad (2.21)$$

The domain, in which $\Phi_a(x_j-x_I) \neq 0$ for all x_j , is called the support of $\Phi_a(x-x_I)$. In this one-dimensional case, the support of $\Phi_a(x-x_I)$ is $]x_I-a, x_I+a[$. The dilatation parameter a is used in Φ_a to control the size of support. In RKPM, the support of $\Phi_a(x-x_I)$ is selected to be a small area such that the shape function $\Psi_I(x)$ associated with node I has interaction with only a small group of surrounding nodes to provide computational efficiency. Also note that $\Psi_I(x)$ does not satisfy the Kronecker delta properties, i.e. $\Psi_I(x_j) \neq \delta_{IJ}$.

The smoothness of the shape function $\Psi_I(x)$ depends greatly on the smoothness of the kernel function Φ_a . Consider a kernel function Φ_a that is m -times continuously differentiable, i.e. $\Phi_a \in C^m(\Omega_x)$; then, the moments defined in Eq. (2.15) are also m -time continuously differentiable and consequently $\tilde{\mathbf{M}} \in C^m(\Omega_x)$. Further, since $\tilde{\mathbf{M}}$ is non-singular, $\tilde{\mathbf{M}}^{-1} = [\det(\tilde{\mathbf{M}})]^{-1} \text{adj } \tilde{\mathbf{M}}$ is also of class $C^m(\Omega_x)$. This leads to the conclusion that $\bar{\Phi}_a(x; x-s) = \Phi_a(x-s) \mathbf{H}^T(0) \tilde{\mathbf{M}}^{-1}(x) \mathbf{H}(x-s) \in C^m(\Omega_x)$ and therefore, $\Psi_I \in C^m(\Omega_x)$. Note that the Gaussian function is $C^\infty(\Omega_x)$ and the cubic spline function is $C^2(\Omega_x)$.

At the end of this section, we would like to point out that for an x that does not locate near the boundary within a distance a , the $\tilde{\mathbf{M}}$ matrix degenerates to a constant matrix in the following form:

$$\tilde{\mathbf{M}} = \int_{-a}^a \mathbf{H}(z) \mathbf{H}^T(z) \Phi_a(z) dz \quad (2.22)$$

if $\mathbf{H}^T(z) = [1, z]$, then $\tilde{\mathbf{M}}$ is a diagonal matrix and consequently the correction function becomes a constant given below:

$$C = \mathbf{H}^T(0) \tilde{\mathbf{M}}^{-1} \mathbf{H}(x-s) = \left[\int_{-a}^a \Phi_a(z) dz \right]^{-1} \quad (2.23)$$

2.2. Numerical integration of $\tilde{\mathbf{M}}$ and $\tilde{\mathbf{M}}_{,x}$

The essential idea behind the development of reproducing conditions is the ability to exactly reproduce polynomials. While the derivation of the correction function (as given in Eq. (2.16)) which contains the $\tilde{\mathbf{M}}$ matrix assures the reproducing conditions, the reproducing equation is discretized to form the shape function. Although the derivation given in [17,18] implies that the integration of $\tilde{\mathbf{M}}$ and $\tilde{\mathbf{M}}_{,x}$ needs to be consistent with the discretization of reproducing equation, we would like to provide a more detailed discussion on the consistency requirement in the discrete sense.

The consistency condition states that if $\mathbf{u}_I^T = \mathbf{H}^T(x_I) = [1, x_I, x_I^2, \dots, x_I^N]$, then the following equation must hold:

$$\sum_{I=1}^{NP} \Psi_I(x) \mathbf{u}_I^T = \mathbf{H}^T(x) = [1, x, x^2, \dots, x^N] \quad (2.24)$$

Substituting the expression of $\Psi_I(x)$ in Eq. (2.23) into Eq. (2.24) leads to

$$\sum_{I=1}^{NP} \Psi_I(x) \mathbf{u}_I^T = \mathbf{H}^T(0) \tilde{\mathbf{M}}^{-1}(x) \sum_{I=1}^{NP} [\mathbf{H}(x - x_I) \mathbf{H}^T(x_I) \Phi_a(x - x_I) \Delta x_I] \quad (2.25)$$

We express $\mathbf{H}^T(x_I)$ in the following form

$$\begin{aligned} \mathbf{H}^T(x_I) &= \mathbf{H}^T(x) - \mathbf{H}^{(1)T}(x)(x - x_I) + \frac{1}{2} \mathbf{H}^{(2)T}(x)(x - x_I)^2 + \dots + \frac{(-1)^N}{N!} \mathbf{H}^{(N)T}(x)(x - x_I)^N \\ &= \mathbf{H}^T(x - x_I) \mathbf{g}(x) \end{aligned} \quad (2.26)$$

where

$$\mathbf{g}^T(x) = \left[\mathbf{H}(x), -\mathbf{H}^{(1)}(x), \frac{1}{2} \mathbf{H}^{(2)}(x), \dots, \frac{(-1)^N}{N!} \mathbf{H}^{(N)}(x) \right] \quad (2.27)$$

and

$$\mathbf{H}^{(i)}(x) \equiv \frac{d^i \mathbf{H}(x)}{dx^i} \quad (2.28)$$

One can rewrite Eq. (2.25) by using Eq. (2.26) to yield

$$\sum_{I=1}^{NP} \Psi_I(x) \mathbf{u}_I^T = \mathbf{H}^T(0) \tilde{\mathbf{M}}^{-1}(x) \sum_{I=1}^{NP} [\mathbf{H}(x - x_I) \mathbf{H}^T(x - x_I) \Phi_a(x - x_I) \Delta x_I] \mathbf{g}(x) \quad (2.29)$$

It can be recognized that in Eq. (2.29), $\sum_{I=1}^{NP} [\mathbf{H}(x - x_I) \mathbf{H}^T(x - x_I) \Phi_a(x - x_I) \Delta x_I]$ is the numerical integration of $\tilde{\mathbf{M}}(x) = \int_{\Omega} \mathbf{H}(x - s) \mathbf{H}^T(x - s) \Phi_a(x - s) ds$, and is denoted by

$$\sum_{I=1}^{NP} [\mathbf{H}(x - x_I) \mathbf{H}^T(x - x_I) \Phi_a(x - x_I) \Delta x_I] \equiv \tilde{\mathbf{M}}^*(x) \quad (2.30)$$

and Eq. (2.29) is rewritten in the following form

$$\sum_{I=1}^{NP} \Psi_I(x) \mathbf{u}_I^T = \mathbf{H}^T(0) \tilde{\mathbf{M}}^{-1}(x) \tilde{\mathbf{M}}^*(x) \mathbf{g}(x) \quad (2.31)$$

Note that the appearance of $\tilde{\mathbf{M}}^*(x)$ in Eq. (2.31) is the result of discretization in the reproducing equation. It is obvious that if only $\tilde{\mathbf{M}}(x)$ is integrated using the same numerical integration method as described in Eq. (2.17), Eq. (2.31) can be reduced to

$$\sum_{I=1}^{NP} \Psi_I(x) \mathbf{u}_I^T = \mathbf{H}^T(0) \mathbf{g}(x) = \mathbf{H}^T(x) \quad (2.32)$$

This result concludes that the matrix $\tilde{\mathbf{M}}(x)$ appearing in the RKPM shape function needs to be

integrated using the same trapezoidal rule as was used in the discretization of the reproducing equation to assure the reproducing conditions.

To determine the appropriate integration method for $\tilde{\mathbf{M}}_{,x}$, we employ the following reproducing condition: If $\mathbf{u}_I^T = \mathbf{H}^T(x_I) = [1, x_I, x_I^2, \dots, x_I^N]$, then

$$\sum_{I=1}^{NP} \Psi_{I,x} \mathbf{u}_I^T = \mathbf{H}_{,x}^T \quad (2.33)$$

Using the property $\tilde{\mathbf{M}}_{,x}^{-1}(x) = -\tilde{\mathbf{M}}_{,x}(x)^{-1} \tilde{\mathbf{M}}(x)_{,x} \tilde{\mathbf{M}}(x)^{-1}$ in conjunction with the explicit expression of $\Psi_{I,x}(x)$ given in Eq. (2.19), one can obtain

$$\begin{aligned} \sum_{I=1}^{NP} \Psi_{I,x}(x) \mathbf{u}_I^T &= \mathbf{H}^T(0) \tilde{\mathbf{M}}^{-1}(x) \left\{ [-\tilde{\mathbf{M}}_{,x}(x) \tilde{\mathbf{M}}^{-1}(x) \tilde{\mathbf{M}}^*(x) + \tilde{\mathbf{M}}_{,x}^*(x)] \mathbf{g}(x) \right. \\ &\quad \left. - \sum_{I=1}^{NP} \mathbf{H}(x - x_I) \mathbf{H}_{,x}^T(x - x_I) \mathbf{g}(x) \Phi_a(x - x_I) \Delta x_I \right\} \end{aligned} \quad (2.34)$$

where

$$\begin{aligned} \tilde{\mathbf{M}}_{,x}^* &= \sum_{I=1}^{NP} [\mathbf{H}_{,x}(x - x_I) \mathbf{H}^T(x - x_I) \Phi_a(x - x_I) + \mathbf{H}(x - x_I) \mathbf{H}_{,x}^T(x - x_I) \Phi_a(x - x_I) \\ &\quad + \mathbf{H}(x - x_I) \mathbf{H}^T(x - x_I) \Phi_{a,x}(x - x_I)] \Delta x_I \end{aligned} \quad (2.35)$$

Note that $\tilde{\mathbf{M}}_{,x}^*$ is exactly the numerical integration of $\tilde{\mathbf{M}}_{,x}$ using the trapezoidal rule. By taking the derivative of Eq. (2.26), the term $\mathbf{H}_{,x}^T(x - x_I) \mathbf{g}(x)$ in Eq. (2.34) can be replaced by

$$\mathbf{H}_{,x}^T(x - x_I) \mathbf{g}(x) = -\mathbf{H}^T(x - x_I) \mathbf{g}_{,x}(x) \quad (2.36)$$

Eq. (2.36) is used to further simplify Eq. (2.34) to obtain

$$\sum_{I=1}^{NP} \Psi_{I,x}(x) \mathbf{u}_I^T = \mathbf{H}^T(0) \tilde{\mathbf{M}}^{-1}(x) \left\{ [-\tilde{\mathbf{M}}_{,x}(x) \tilde{\mathbf{M}}^{-1}(x) \tilde{\mathbf{M}}^*(x) + \tilde{\mathbf{M}}_{,x}^*(x)] \mathbf{g}(x) + \tilde{\mathbf{M}}^*(x) \mathbf{g}_{,x}(x) \right\} \quad (2.37)$$

Only if one integrates $\tilde{\mathbf{M}}(x)$ and $\tilde{\mathbf{M}}_{,x}(x)$ using Eqs. (2.30) and (2.35), can Eq. (2.37) degenerate to

$$\sum_{I=1}^{NP} \Psi_{I,x}(x) \mathbf{u}_I^T = \mathbf{H}^T(0) \mathbf{g}_{,x}(x) = \mathbf{H}_{,x}^T(x) \quad (2.38)$$

This result indicates that to satisfy the reproducing conditions on the first-order derivative of the polynomial, $\tilde{\mathbf{M}}(x)$ and $\tilde{\mathbf{M}}_{,x}(x)$ need to be integrated using the same trapezoidal rule as was used to discretize the reproducing equation.

2.3. Multi-dimensional RKPM shape function

This section extends the one-dimensional RKPM shape function to multi-dimensional. The multi-dimensional kernel function can be constructed by replacing Eq. (2.4) in the following form:

$$\Phi_a(d_I) = \frac{1}{a} \Phi\left(\frac{d_I}{a}\right) \quad (2.39)$$

where

$$d_I = \|\mathbf{x} - \mathbf{x}_I\| \quad (2.40)$$

or simply by performing products of one-dimensional kernel functions

$$\Phi_a(\mathbf{x} - \mathbf{x}_I) = \prod_{i=1}^{n_{sd}} \frac{1}{a_i} \Phi\left(\frac{x_i - x_{Ii}}{a_i}\right) \quad (2.41)$$

where n_{sd} is the number of spatial dimensions and a_i is the dimension parameter in the i th dimension. The multi-dimensional correction function is expressed by

$$C(\mathbf{x}; \mathbf{x} - \mathbf{x}_I) = \mathbf{H}^T(\mathbf{x} - \mathbf{x}_I) \mathbf{b}(\mathbf{x}) \quad (2.42)$$

where \mathbf{H} is the multi-dimensional basis function vector that is expressed by

$$\mathbf{H}(\mathbf{x} - \mathbf{x}_I) = [1, x_1 - x_{1I}, x_2 - x_{2I}, \dots, (x_{n_{sd}} - x_{n_{sd}I})^N] \quad (2.43)$$

By imposing the completeness requirement, one can obtain $\mathbf{b}(\mathbf{x})$ by

$$\mathbf{b}(\mathbf{x}) = \tilde{\mathbf{M}}^{-1}(\mathbf{x}) \mathbf{H}(\mathbf{0}) \quad (2.44)$$

where

$$\tilde{\mathbf{M}}(\mathbf{x}) = \int_{\Omega} \mathbf{H}(\mathbf{x} - \mathbf{s}) \mathbf{H}^T(\mathbf{x} - \mathbf{s}) d\mathbf{s}_1 \cdots d\mathbf{s}_{n_{sd}} \quad (2.45)$$

Consequently, the correction function and the modified kernel function are

$$C(\mathbf{x}; \mathbf{x} - \mathbf{x}_I) = \mathbf{H}^T(\mathbf{0}) \tilde{\mathbf{M}}^{-1}(\mathbf{x}) \mathbf{H}(\mathbf{x} - \mathbf{x}_I) \quad (2.46)$$

$$\bar{\Phi}_a(\mathbf{x}; \mathbf{x} - \mathbf{x}_I) = C(\mathbf{x}; \mathbf{x} - \mathbf{x}_I) \Phi_a(\mathbf{x} - \mathbf{x}_I) \quad (2.47)$$

Finally, the multi-dimensional reproducing equation is discretized to obtain the following multi-dimensional RKPM shape function:

$$\Psi_I(\mathbf{x}) = \bar{\Phi}_a(\mathbf{x}; \mathbf{x} - \mathbf{x}_I) \Delta V_I = \mathbf{H}^T(\mathbf{0}) \tilde{\mathbf{M}}^{-1}(\mathbf{x}) \mathbf{H}(\mathbf{x} - \mathbf{x}_I) \Phi_a(\mathbf{x} - \mathbf{x}_I) \Delta V_I \quad (2.48)$$

where ΔV_I is the volume associated with particle I .

3. Non-linear RKPM formulation

In this section we consider the RKPM formulation of the basic equations of our model problems. Emphasis is placed on the RKPM discretization of general large deformation problems including geometric and material non-linearities. The crucial point is to realize that we discretize the domain of interest by a set of particles that are not connected by a mesh. Since the RKPM shape function defined at each particle does not possess Kronecker delta properties, the essential boundary conditions and externally applied forces need to be properly treated.

3.1. Problem statement and variational equation

Consider a body which initially occupies a region Ω_X with boundary Γ_X , and is deformed from its initial configuration to a deformed configuration Ω_x with deformed boundary Γ_x . The body is subjected to body force b_i in Ω_x , surface traction h_i on the natural boundary $\Gamma_x^{h_i}$, and prescribed displacement g_i on the essential boundary $\Gamma_x^{g_i}$. We use a fixed Cartesian coordinate system, and denote the particle positions in the initial configuration Ω_X by \mathbf{X} and those in the deformed configuration Ω_x at time t by a mapping function $\boldsymbol{\varphi}$ where

$$\mathbf{x} = \boldsymbol{\varphi}(\mathbf{X}, t) \quad (3.1)$$

The mapping is one-to-one and hence in each domain of regularity, the determinate of deformation gradient $J = \det(\partial x_i / \partial X_j)$ is neither zero nor infinite. The motion of the body is governed by the equation of motion with initial conditions. Our model problem is as follows: Given $b_i(\mathbf{x})$, $h_i(\mathbf{x})$, $g_i(\mathbf{x})$, $u_i^0(\mathbf{X})$, $v_i^0(\mathbf{X})$, find $u_i(\mathbf{X}, t)$ such that they satisfy

$$\rho \ddot{u}_i = \tau_{ij,j} + b_i \quad \text{in } \Omega_x \quad (3.2)$$

with boundary conditions

$$\tau_{ij} n_j = h_i \quad \text{on } \Gamma_x^{h_i} \quad (3.3)$$

$$u_i = g_i \quad \text{on } \Gamma_x^{g_i} \quad (3.4)$$

and initial conditions

$$u_i(X, 0) = u_i^0(X) \quad (3.5)$$

$$\dot{u}_i(X, 0) = v_i^0(X) \quad (3.6)$$

where ρ is the density, n_i is the surface outward normal in the current configuration, u_i^0 is the initial displacement, v_i^0 is the initial velocity, $\dot{f} \equiv \partial f / \partial t|_{[X]}$ is the material time derivative, $f_{,i} \equiv \partial f / \partial x_i$ is the spatial derivative, $u(X, t) = \varphi(X, t) - X = x(X, t) - X$ is the material displacement, and τ_{ij} is Cauchy stress obtained from the constitutive law. For a hyperelastic material, the second Piola–Kirchhoff stress S_{ij} is calculated from the strain energy density function W by

$$S_{ij} = \frac{\partial W}{\partial E_{ij}} \quad (3.7)$$

then the second Piola–Kirchhoff stress is related to the Cauchy stress by

$$\tau_{ij} = \frac{1}{J} F_{im} S_{mn} F_{jn} \quad (3.8)$$

For path-dependent elasto-plasticity, the Jaumann Cauchy stress rate is obtained by the following constitutive equation

$$\dot{\tau}_{ij} = C_{ijkl}^c v_{[k,l]} + R_{ijkl} v_{(k,l)} \quad (3.9)$$

where $v_{[k,l]}$ and $v_{(k,l)}$ are the symmetric and anti-symmetric parts of velocity gradient $\partial v_i / \partial x_j$, respectively, and C_{ijkl}^c is the co-rotational material response tensor which is material dependent, and R_{ijkl} is given by

$$R_{ijkl} = \frac{1}{2} (\tau_{il} \delta_{jk} + \tau_{jl} \delta_{ik} - \tau_{ik} \delta_{jl} - \tau_{jk} \delta_{il}) \quad (3.10)$$

The variational equation is formulated as follows: Given $b_i(x)$, $h_i(x)$, $g_i(x)$, $u_i^0(X)$, $v_i^0(X)$, find $u_i(X, t) \in H_g^1$ ($H_g^1 = \{v : v \in H^1, v_i = g_i \text{ on } \Gamma_x^{g_i}\}$), such that for all $\delta u_i \in H_0^1$ ($H_0^1 = \{v : v \in H^1, v_i = 0 \text{ on } \Gamma_x^{g_i}\}$), the following equation is satisfied:

$$\int_{\Omega_x} \delta u_i \rho \ddot{u}_i d\Omega + \int_{\Omega_x} \delta u_{i,j} \tau_{ij} d\Omega - \int_{\Omega_x} \delta u_i b_i d\Omega - \int_{\Gamma_x^{h_i}} \delta u_i h_i d\Gamma = 0 \quad (3.11)$$

with

$$u_i(X, 0) = u_i^0(X) \quad (3.12)$$

$$\dot{u}_i(X, 0) = v_i^0(X) \quad (3.13)$$

where H^1 is the Sobolev space of degree one, and τ_{ij} is obtained from constitutive equations discussed previously. In Lagrangian formulation, mass conservation is automatically satisfied and therefore is more convenient to transform the first term in Eq. (3.11) to the initial configuration

$$\int_{\Omega_x} \delta u_i \rho \ddot{u}_i d\Omega = \int_{\Omega_X} \delta u_i \rho^0 \ddot{u}_i d\Omega \quad (3.14)$$

where ρ^0 is the initial density. For hyperelastic material, since the second Piola–Kirchhoff stress can be

directly calculated following Eq. (3.7), it is more effective to express the second term in Eq. (3.11) using the second Piola–Kirchhoff stress in the initial configuration by

$$\int_{\Omega_x} \delta u_{i,j} \tau_{ij} d\Omega = \int_{\Omega_X} \delta E_{ij} S_{ij} d\Omega = \int_{\Omega_X} \delta u_{i,j} F_{ik} S_{kj} d\Omega \quad (3.15)$$

where E_{ij} is the Green Lagrangian strain, $u_{i,j} \equiv \partial u_i / \partial x_j$, $u_{i,j} \equiv \partial u_i / \partial X_j$ and $F_{ik} S_{kj}$ is indeed the first Piola–Kirchhoff stress.

For non-linear problems, linearization of Eq. (3.11) is required. We rewrite Eq. (3.11) in the following form:

$$\Theta_1 + \Theta_2 - \Theta_3 - \Theta_4 = 0 \quad (3.16)$$

where

$$\Theta_1 = \int_{\Omega_X} \delta u_i \rho^0 \ddot{u}_i d\Omega \quad (3.17)$$

$$\Theta_2 = \int_{\Omega_X} \delta u_{i,j} F_{ik} S_{kj} d\Omega \quad (\text{for hyperelasticity}) \quad (3.18)$$

$$= \int_{\Omega_x} \delta u_{i,j} \tau_{ij} d\Omega \quad (\text{for elasto-plasticity}) \quad (3.19)$$

$$\Theta_3 = \int_{\Omega_x} \delta u_i b_i d\Omega \quad (3.20)$$

$$\Theta_4 = \int_{\Gamma^{h_i}} \delta u_i h_i d\Gamma \quad (3.21)$$

To handle geometric and material non-linearities, we shall consider an incremental equation of motion. Let n and ν denote time step and iteration counters, respectively, and neglecting the load correction tangent operator due to deformation dependent surface traction, the incremental equation is

$$\Delta \Theta_1 + \Delta \Theta_2 = (\Theta_3 + \Theta_4)_{n+1} - (\Theta_1 + \Theta_2)_{n+1}^{\nu+1} \quad (3.22)$$

where $\Delta \Theta_1$ and $\Delta \Theta_2$ are the linearization of Θ_1 and Θ_2 , respectively, and they are given by

$$\Delta \Theta_1 = \int_{\Omega_X} \delta u_i \rho^0 \Delta \ddot{u}_i d\Omega \quad (3.23)$$

$$\Delta \Theta_2 = \int_{\Omega_X} \delta u_{i,j} (D_{ijkl}^S + T_{ijkl}^S) \Delta u_{k,l} d\Omega \quad (\text{for hyperelasticity}) \quad (3.24)$$

$$= \int_{\Omega_x} \delta u_{i,j} (D_{ijkl}^\tau + T_{ijkl}^\tau) \Delta u_{k,l} d\Omega \quad (\text{for elasto-plasticity}) \quad (3.25)$$

and

$$D_{ijkl}^\tau = C_{ijkl}^c + \tau_{ij} \delta_{kl} - \frac{1}{2} (\tau_{il} \delta_{jk} + \tau_{jl} \delta_{ik} + \tau_{ik} \delta_{jl} + \tau_{jk} \delta_{il}) \quad (3.26)$$

$$T_{ijkl}^\tau = \tau_{jl} \delta_{ik} \quad (3.27)$$

$$D_{ijkl}^S = F_{ip} F_{kq} \frac{\partial^2 W}{\partial E_{pj} \partial E_{ql}} \quad (3.28)$$

$$T_{ijkl}^S = S_{jl} \delta_{ik} \quad (3.29)$$

3.2. Material kernel function

In the analysis of structures, Lagrangian formulation as described in the previous section usually represents a more natural and effective approach, in which attention is focused on the motion of material particles through a volume that deforms with the structure. The reference configuration in the variational equation can be selected as the current configuration or the initial configuration, depending on the choice of stress and strain measures. Note that in the RKPM approach, the kernel functions are constructed at the global coordinate. The value of the shape function of a given node I is determined by the distance between any point of evaluation in space and node I . It is therefore important to decide in which configuration should the particle distance be measured to define the kernel function in a large deformation analysis.

In dealing with path-independent materials such as hyperelastic material, the total quantity of second Piola–Kirchhoff stress can be directly calculated from strain energy density function without going through an integration process. In this case, the material-based stress and strain measures are used more conveniently in computation, and consequently the initial configuration is selected as the reference configuration as shown in Eq. (3.18). The kernel function is defined using the measure of ‘material’ distance by

$$\Phi_a^X(X - X_I) = \frac{1}{a} \Phi\left(\frac{\|X - X_I\|}{a}\right) \quad (3.30)$$

We call this kernel function defined by the measure of material distance the material kernel function, and is denoted by $\Phi_a^X(X - X_I)$ with subscript ‘ X ’. The RKPM material shape function is then constructed by

$$\Psi_I(X) = H^T(\mathbf{0}) \tilde{M}^{-1}(X) H(X - X_I) \Phi_a^X(X - X_I) \Delta V_I \quad (3.31)$$

where

$$M(X) = \int_{\Omega_X} H(X - S) H^T(X - S) dS \quad (3.32)$$

and the basis function vector H is also constructed at a material coordinate. For path-dependent materials such as elasto-plasticity, the Cauchy stress rate is given in the current configuration and integration needs to be performed to obtain the total Cauchy stress quantities. The variational equation is usually formed in the current configuration as given in Eq. (3.19). Note that the selection of reference configuration is arbitrary and the selection lies in its convenience. For elasto-plasticity, the material kernel function is constructed by mapping the position vector in the current configuration x to $X = \varphi^{-1}(x, t)$ for the measure of material distance to yield

$$\Phi_a^X(\varphi^{-1}(x, t) - \varphi^{-1}(x_I, t)) = \frac{1}{a} \Phi\left(\frac{\|\varphi^{-1}(x, t) - \varphi^{-1}(x_I, t)\|}{a}\right) \quad (3.33)$$

and similarly, Eq. (3.31) is used to form the material shape function with the material coordinate calculated by $X = \varphi^{-1}(x, t)$. In fact, since all the kinematic and kinetic quantities are evaluated at fixed material particles in Lagrangian computation, the inverse mapping $X = \varphi^{-1}(x, t)$ actually requires no computation.

For path-dependent materials, the calculation of Cauchy stress in Eq. (3.9) requires the computation of velocity gradient, and thus the spatial derivative of material shape function needs to be performed by

$$\frac{\partial \Psi_I(X)}{\partial x_i(X, t)} = \frac{\partial \Psi_I(X)}{\partial X_j} F_{ji}^{-1}(x(X, t)) \quad (3.34)$$

where F^{-1} is obtained by performing the inverse of F to avoid taking spatial derivative of the material shape functions.

The characteristics of material kernel function can be illustrated in a simple one-dimensional uniaxial tension problem with the material deformation given by the following function

$$x = \varphi(X, t) = (1 + t)X \quad (3.35)$$

The material kernel function is expressed by

$$\Phi_a^X = \frac{1}{a} \Phi\left(\frac{|X - X_I|}{a}\right) = \frac{1}{a} \Phi\left(\frac{|x - x_I|}{(1+t)a}\right) \quad (3.36)$$

The shapes of this material kernel function (cubic spline) plotted in the undeformed and deformed configuration are shown in Fig. 1. The support of the function covers the same set of particles throughout the deformation with a fixed a and therefore is classified as a 'Lagrangian-typed' kernel function that naturally fits into a Lagrangian formulation.

3.3. Kinematically admissible RKPM shape functions

The essential boundary conditions of the model problem can be introduced either by the use of the Lagrange multiplier method, or by the appropriate selection of kinematically admissible test and trial functions in the variational equation. The first approach requires the solution of independent kinematic variables as well as Lagrange multipliers at each incremental step. The second approach can be achieved by the reconstruction of RKPM shape functions that possess Kronecker delta properties. This development allows the direct treatment of boundary conditions and hence the kinematically admissible test and trial functions can be formed.

The displacement in the variational equation is approximated by RKPM shape function in the following form:

$$u_i^a(X, t) = \sum_{I=1}^{NP} \Psi_I(X) d_{iI}(t) \quad (3.37)$$

where ' a ' refers to the RKPM shape function with support measured by the dilation parameter a . The displacement $u_i^a(X, t)$ has to satisfy the following conditions:

$$u_i^a(X_I, t) = g_i(X_I, t) \quad \forall I \in \eta_{g_i} \quad (3.38)$$

$$\delta u_i^a(X_I, t) = 0 \quad \forall I \in \eta_{g_i} \quad (3.39)$$

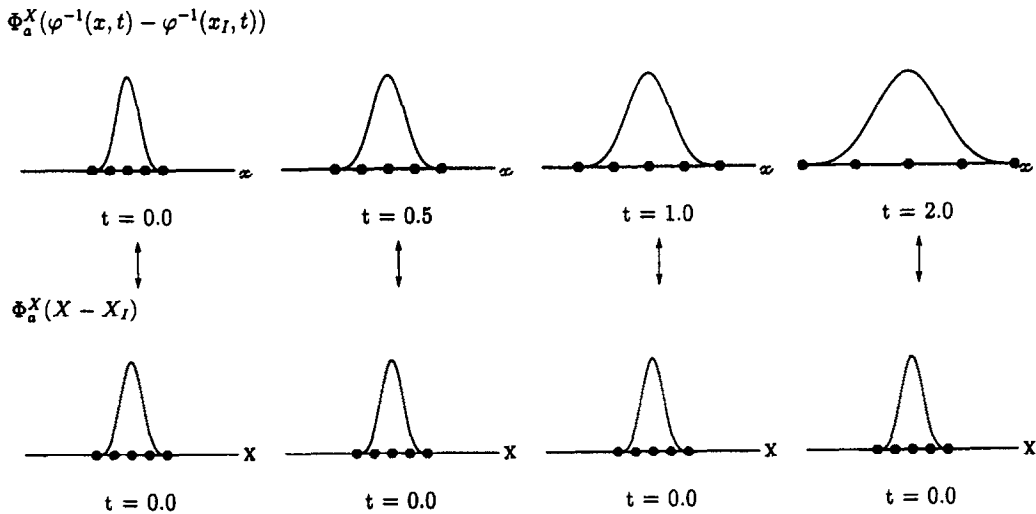


Fig. 1. Material kernel function.

where η_{g_i} denotes a set of particle numbers in which the associated particles are located on $\Gamma_{X_i}^{g_i}$. Eqs. (3.38) and (3.39) represent two sets of constraint equations that are difficult to solve simultaneously with the equation of motion. In this section, we shall reconstruct the kinematically admissible RKPM shape functions such that they satisfy Eqs. (3.38) and (3.39).

We first establish the relationship between the nodal value $u_i^a(X_j, t)$ and the ‘generalized’ displacement $d_{iJ}(t)$. Letting $\hat{d}_{iJ}(t) \equiv u_i^a(X_j, t)$ be the nodal value of $u_i^a(X, t)$ at X_j , we have the following conditions:

$$\hat{d}_{iJ}(t) = \sum_{I=1}^{NP} \Psi_I(X_j) d_{iI}(t) = \sum_{I=1}^{NP} L_{IJ} d_{iI}(t) \quad (3.40)$$

or

$$d_{iI}(t) = \sum_{K=1}^{NP} L_{IK}^{-T} \hat{d}_{iK}(t) \quad (3.41)$$

where

$$L_{IJ} = \Psi_I(X_j) \quad (3.42)$$

By substituting Eq. (3.41) into Eq. (3.37), one can obtain

$$u_i^a(X, t) = \sum_{I=1}^{NP} \Psi_I(X) d_{iI}(t) = \sum_{I=1}^{NP} \sum_{K=1}^{NP} \Psi_I(X) L_{IK}^{-T} \hat{d}_{iK}(t) \equiv \sum_{K=1}^{NP} \hat{\Psi}_K(X) \hat{d}_{iK}(t) \quad (3.43)$$

where

$$\hat{\Psi}_K(X) = \sum_{I=1}^{NP} L_{KI}^{-1} \Psi_I(X) \quad (3.44a)$$

Note that

$$\hat{\Psi}_I(X_j) = \sum_{K=1}^{NP} L_{IK}^{-1} \Psi_K(X_j) = \sum_{K=1}^{NP} L_{IK}^{-1} L_{KJ} = \delta_{IJ} \quad (3.44b)$$

With this modified RKPM shape function, the admissible trial and test functions for the variation equation can be constructed by

$$u_i^a(X, t) = \sum_{K=1}^{NP} \hat{\Psi}_K(X) \hat{d}_{iK}(t) \quad (3.45)$$

$$\delta u_i^a(X, t) = \sum_{K=1}^{NP} \hat{\Psi}_K(X) \delta \hat{d}_{iK}(t) \quad (3.46)$$

where

$$\hat{d}_{iI}(t) = g_i(X_I, t) \quad \forall I \in \eta_{g_i} \quad (3.47)$$

$$\delta d_{iI}(t) = 0 \quad \forall I \in \eta_{g_i} \quad (3.48)$$

The velocity and acceleration are approximated by

$$\dot{u}_i(X, t) = \sum_{I=1}^{NP} \hat{\Psi}_I(X) \dot{\hat{d}}_{iI}(t) \quad (3.49)$$

$$\ddot{u}_i(X, t) = \sum_{I=1}^{NP} \hat{\Psi}_I(X) \ddot{\hat{d}}_{iI}(t) \quad (3.50)$$

Although the construction of the modified shape functions requires additional effort to compute L^{-1} , this transformation matrix is formed once and for all if the displacement is expressed by the material coordinate, whereas using the Lagrange multiplier method the Lagrange multipliers need to be solved

at every incremental step. It is also noted that the transformation matrix needs to be formed only for those shape functions where their supports interact with the essential boundaries.

3.4. RKPM matrix equations

To approximate kinematic variables using RKPM material shape functions, we rewrite the variational incremental equation for path-independent and path-dependent materials by rearranging Θ_2 , Θ_3 , Θ_4 and $\Delta\Theta_2$ as follows:

$$\Theta_2 = \int_{\Omega_X} \delta u_{i,j}(X, t) \sigma_{ij}(X, t) d\Omega \quad (3.51)$$

$$\Theta_3 = \int_{\Omega_X} \delta u_i(X, t) b_i(x(X, t)) J(X, t) d\Omega \quad (3.52)$$

$$\Theta_4 = \int_{\Gamma_X^{h_i}} \delta u_i(X, t) h_i^0(X, t) d\Gamma \quad (3.53)$$

$$\Delta\Theta_2 = \int_{\Omega_X} \delta u_{i,j}(X, t) [D_{ijkl}(X, t) + T_{ijkl}(X, t)] \Delta u_{k,l}(X, t) d\Omega \quad (3.54)$$

where h^0 is the surface force per unit undeformed area on the undeformed natural boundary $\Gamma_X^{h_i}$, and $\sigma_{ij}(X, t)$, $D_{ijkl}(X, t)$ and $T_{ijkl}(X, t)$ for hyperelastic and elasto-plastic materials are given in Table 1.

Due to the use of material shape function, the deformation gradient is calculated by

$$F_{ij}(X, t) = \sum_{I=1}^{NP} \left[\frac{\partial \Psi_I(X)}{\partial X_j} d_{iI}(t) \right] + \delta_{ij} = \sum_{I=1}^{NP} \left[\frac{\partial \hat{\Psi}_I(X)}{\partial X_j} \hat{d}_{iI}(t) \right] + \delta_{ij} \quad (3.55)$$

Note that for path-dependent materials, F^{-1} is calculated from the inverse of F to avoid taking a spatial derivative of the material shape function. The matrix equation can be obtained by introducing RKPM shape function to Eqs. (3.22) to yield

$$\hat{M} \Delta \hat{\hat{d}} + \hat{K} \Delta \hat{d} = \Delta \hat{f} \quad (3.56)$$

It should be noted that the matrices \hat{M} , \hat{K} and $\Delta \hat{f}$ can be constructed directly by using the modified RKPM shape functions $\hat{\Psi}_I$ and its derivatives, or by utilizing the relation between $d(t)$ and $\hat{d}(t)$ given by

$$d(t) = A^{-T} \hat{d}(t) \quad (3.57)$$

where

$$A_{IJ} = \Psi_I(X_J) I \quad (3.58)$$

and form the matrices \hat{M} , \hat{K} and $\Delta \hat{f}$ by using the coordinate transformation rule as follows

Table 1
 $\sigma_{ij}(X, t)$, $D_{ijkl}(X, t)$ and $T_{ijkl}(X, t)$ for hyperelastic and elasto-plastic materials

	Hyperelastic	Elasto-plastic
σ_{ij}	$F_{ik}(X, t) S_{kj}(X, t)$	$J(X, t) F_{jk}^{-1}(x(X, t)) \tau_{jk}(x(X, t))$, $J(X, t) = \det(F(X, t))$
D_{ijkl}	$D_{ijkl}^s(X, t)$	$J(X, t) F_{jp}^{-1}(x(X, t)) F_{lq}^{-1}(x(X, t)) D_{ipkq}^*(x(X, t))$
T_{ijkl}	$T_{ijkl}^s(X, t)$	$J(X, t) F_{jp}^{-1}(x(X, t)) F_{lq}^{-1}(x(X, t)) T_{ipkq}^*(x(X, t))$

$$\hat{\mathbf{M}} = \mathbf{A}^{-1} \mathbf{M} \mathbf{A}^{-\mathrm{T}} \quad (3.59)$$

$$\hat{\mathbf{K}} = \mathbf{A}^{-1} \mathbf{K} \mathbf{A}^{-\mathrm{T}} \quad (3.60)$$

$$\Delta \hat{\mathbf{f}} = \mathbf{A}^{-1} \Delta \mathbf{f} \quad (3.61)$$

$$\Delta \hat{\mathbf{d}} = \mathbf{A} \Delta \mathbf{d} \quad (3.62)$$

$$M_{IJ} = \int_{\Omega_X} \rho^0 \Psi_I \Psi_J \, \mathrm{d}\Omega \quad (3.63)$$

$$\mathbf{K} = \mathbf{K}^M + \mathbf{K}^G \quad (3.64)$$

$$\Delta \mathbf{f} = (\mathbf{f}^{\text{ext}})_{n+1} - (\mathbf{f}^{\text{int}})_{n+1}^v \quad (3.65)$$

$$\mathbf{K}_{IJ}^G = \int_{\Omega_X} \mathbf{B}_I^{G\mathrm{T}} \mathbf{T} \mathbf{B}_J^G \, \mathrm{d}\Omega \quad (3.66)$$

$$\mathbf{K}_{IJ}^M = \int_{\Omega_X} \mathbf{B}_I^{M\mathrm{T}} \mathbf{D} \mathbf{B}_J^M \, \mathrm{d}\Omega \quad (3.67)$$

$$\mathbf{f}_I^{\text{ext}} = \int_{\Omega_X} \Psi_I \mathbf{b} \, \mathrm{d}\Omega + \int_{\Gamma_X^{h_I}} \Psi_I \mathbf{h}^0 \, \mathrm{d}\Gamma \quad (3.68)$$

$$\mathbf{f}_I^{\text{int}} = \int_{\Omega_X} \mathbf{B}^{G\mathrm{T}} \mathbf{\Xi} \, \mathrm{d}\Omega \quad (3.69)$$

For two-dimensional problems,

$$\mathbf{B}_I^G = \begin{bmatrix} \frac{\partial \Psi_I}{\partial X_1} & 0 \\ 0 & \frac{\partial \Psi_I}{\partial X_2} \\ \frac{\partial \Psi_I}{\partial X_2} & 0 \\ 0 & \frac{\partial \Psi_I}{\partial X_1} \\ \varepsilon \frac{\Psi_I}{X_I} & 0 \end{bmatrix} \quad (3.70)$$

$$\mathbf{B}_I^M = \begin{bmatrix} \frac{\partial \Psi_I}{\partial X_1} & 0 \\ 0 & \frac{\partial \Psi_I}{\partial X_2} \\ \frac{\partial \Psi_I}{\partial X_2} & \frac{\partial \Psi_I}{\partial X_1} \\ \varepsilon \frac{\Psi_I}{X_I} & 0 \end{bmatrix} \quad (3.71)$$

$$\varepsilon = \begin{cases} 1 & \text{for axisymmetric} \\ 0 & \text{for plane strain} \end{cases} \quad (3.72)$$

The matrices D , T and the vector Ξ are constructed from D_{ijkl} , T_{ijkl} and σ_{ij} as given in Table 1, respectively. With this method, the force vector given in Eq. (3.61) is the nodal force vector, and the point load can also be directly applied to the structure.

4. Numerical procedures

To perform the integration in Eqs. (3.63) and (3.66) through (3.69) using Gauss quadrature rules, the domain is subdivided into integration zones that are defined independent to the RKPM particles as shown in Fig. 2. The Gauss integration points are defined in each integration zone. Each integration point could be covered by the supports of several shape functions. As illustrated in Fig. 2, the integration point A is covered by the supports of shape functions associated with particles I , J and K . For each integration point A , we define a set S^A that contains all the particles in which their supports of shape functions cover integration point A , for example, $S^A = \{I, J, K\}$ in Fig. 2.

4.1. Computation of stresses and strains

Due to the use of material shape function, Green–Lagrangian strain and second Piola–Kirchhoff stress can be directly calculated in hyperelasticity, whereas in elasto-plasticity the inverse of the deformation gradient is an additional quantity that needs to be calculated for Cauchy stress computation. The following flowchart describes the calculation of strains and stresses at integration point X_A :

(1) Loop over each particle I belongs to S^A :

- (a) Compute $\Psi_I(X_A)$ and $\Psi_{I,j}(X_A)$.
- (b) Compute deformation gradient

$$F_{ij}(X_A, t) \leftarrow F_{ij}(X_A, t) + \Psi_{I,j}(X_A) d_{it}(t).$$

End of loop.

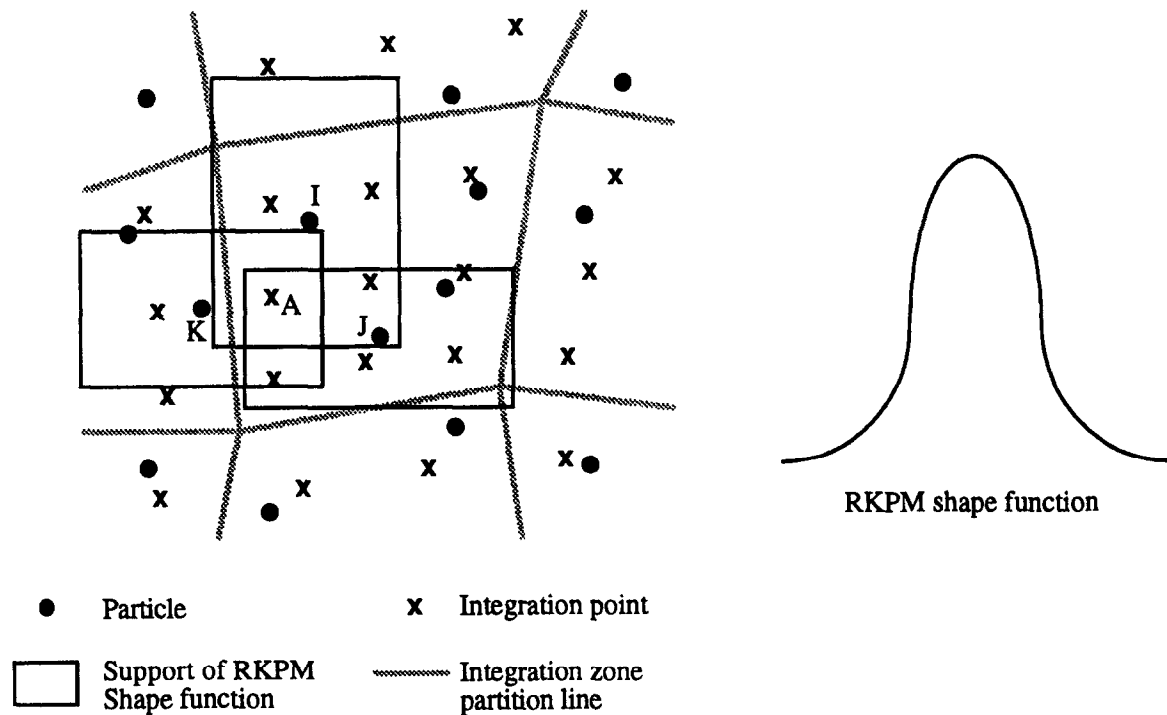


Fig. 2. Graphical representation of RKPM discretization.

(2) *For hyperelasticity:*

Compute Green–Lagrangian strain $E(X_A, t)$ and invariants of Green deformation tensor.

For elasto-plasticity:

(a) Compute $F^{-1}(x(X_A, t))$.

(b) Loop over each particle I belongs to S^A :

Compute velocity gradient:

$$v_{i,j}(x(X_A, t)) \leftarrow v_{i,j}(x(X_A, t)) + \Psi_{I,\bar{k}}(X_A) F_{kI}^{-1}(x(X_A, t)) \dot{d}_{iI}(t)$$

End of Loop

(3) Compute second Piola–Kirchhoff stress $S(X_A, t)$ described in Appendix A or Cauchy stress $\tau(x(X_A, t))$ described in Appendix B.

4.2. Integration of mass matrix, stiffness matrix and force vector

Since the RKPM shape functions are defined at a global level and they have compact support, the construction of mass and stiffness matrices and force vectors is slightly different from that of finite elements. In this work, Gauss quadrature rules are used for domain (boundary) integration, and the domain is subdivided into integration zones. The flow chart is given below:

(1) Loop over each integration zone:

(a) Loop over each integration point X_A :

(I) For hyperelasticity, compute $F(X_A, t)$ and $S(X_A, t)$.

For elasto-plasticity, compute $F^{-1}(X_A, t)$ and $\tau(x(X_A, t))$.

(II) Form $\Xi(X_A, t)$, $D(X_A, t)$ and $T(X_A, t)$ according to Eqs. (3.26)–(3.29) and Appendices A and B.

(III) Loop over each particle $I \in S^A$:

(i) Form $\Psi_I(X_A)$, $B_I^G(X_A, t)$ and $B_I^M(X_A, t)$.

(ii) Form f_I^{ext} , f_I^{int} and assemble $\Delta f_I = f_I^{\text{ext}} - f_I^{\text{int}}$.

(iii) Loop over each particle $J \in S^A$:

Form $\Psi_J(X_A)$, $B_J^G(X_A, t)$ and $B_J^M(X_A, t)$.

Form K_{IJ}^G, K_{IJ}^M and M_{IJ} .

Assemble $K_{IJ} = K_{IJ}^G + K_{IJ}^M$ and M_{IJ} .

End particle loop J .

End particle loop I .

End integration point loop.

End integration zone loop.

(2) Form transformation matrix Λ .

(3) Form \hat{M} , \hat{K} and $\Delta \hat{f}$.

4.3. Time integration procedures

The Newmark method is used for temporal discretization of Eq. (3.56). Let \hat{d}_n , \hat{v}_n and \hat{a}_n be the temporal discretization of $\hat{d}(t_n)$, $\dot{\hat{d}}(t_n)$ and $\ddot{\hat{d}}(t_n)$, respectively. The Newmark time integration procedures are given as follows:

(1) Initialization:

(a) Form \hat{M} , \hat{K} and \hat{f}^{ext}

(b) Compute the initial nodal acceleration \hat{a}^0 from the initial nodal displacement \hat{d}^0 by

$$\hat{M} \hat{a}^0 = \hat{f}^{\text{ext}} - \hat{K} \hat{d}^0 \quad (4.1)$$

(2) At $(n+1)$ th time step and $(v+1)$ th iteration

(a) Predictor phase at $v=0$:

$$\tilde{d}_{n+1}^{v+1} = \hat{d}_n + \Delta t \hat{v}_n + \frac{\Delta t^2}{2} (1 - 2\beta) \hat{a}_n \quad (4.2)$$

$$\tilde{\mathbf{v}}_{n+1}^{\nu+1} = \hat{\mathbf{v}}_n + (1 - \gamma) \Delta t \hat{\mathbf{a}}_n \quad (4.3)$$

$$\tilde{\mathbf{a}}_{n+1}^{\nu+1} = \hat{\mathbf{a}}_n \quad (4.4)$$

- (b) Compute stress predictor $\tilde{\mathbf{S}}_{n+1}^{\nu+1} = \mathbf{S}(\tilde{\mathbf{d}}_{n+1}^{\nu+1})$ or $\tilde{\boldsymbol{\tau}}_{n+1}^{\nu+1} = \boldsymbol{\tau}(\tilde{\mathbf{d}}_{n+1}^{\nu+1})$.
 (c) Compute $\hat{\mathbf{K}}_{n+1}^{\nu+1}$, $(\hat{\mathbf{f}}^{\text{ext}})_{n+1}^{\nu+1}$ and $(\hat{\mathbf{f}}^{\text{int}})_{n+1}^{\nu+1}$ from predictors.
 (d) Solve for $\Delta \hat{\mathbf{a}}$:

$$(\hat{\mathbf{M}} + \beta \Delta t^2 \hat{\mathbf{K}}_{n+1}^{\nu+1}) \Delta \hat{\mathbf{a}} = (\hat{\mathbf{f}}^{\text{ext}} - \hat{\mathbf{f}}^{\text{int}} - \hat{\mathbf{M}} \tilde{\mathbf{a}})_{n+1}^{\nu+1} \quad (4.5)$$

- (e) Corrector phase:

$$\hat{\mathbf{a}}_{n+1}^{\nu+1} = \hat{\mathbf{a}}_{n+1}^{\nu} + \Delta \hat{\mathbf{a}} \quad (4.6)$$

$$\hat{\mathbf{v}}_{n+1}^{\nu+1} = \hat{\mathbf{v}}_n + (1 - \gamma) \Delta t \hat{\mathbf{a}}_n + \gamma \Delta t \hat{\mathbf{a}}_{n+1}^{\nu+1} \quad (4.7)$$

$$\hat{\mathbf{d}}_{n+1}^{\nu+1} = \hat{\mathbf{d}}_n + \Delta t \hat{\mathbf{v}}_n + \frac{\Delta t^2}{2} (1 - 2\beta) \hat{\mathbf{a}}_n + \beta \Delta t^2 \hat{\mathbf{a}}_{n+1}^{\nu+1} \quad (4.8)$$

- (f) Update second Piola–Kirchhoff stress $\mathbf{S}_{n+1}^{\nu+1}$ or Cauchy stress $\boldsymbol{\tau}_{n+1}^{\nu+1}$.
 (g) Convergence check.
 If yes, set $n + 1 \leftarrow n$ and go to (a) in step (2).
 If no, set $\nu + 1 \leftarrow \nu$, predictors \leftarrow correctors and go to (b) in step (2).

5. RKPM mass lumping

For explicit time integration, we perform a row-sum method to construct a lumped mass. To be consistent with the incremental equation expressed in the nodal coordinate, the lumped mass matrix is formed at a nodal coordinate. The consistent mass matrix $\hat{\mathbf{M}}$ given in Eq. (3.59) can be rewritten in the following form:

$$\hat{\mathbf{M}}_{IJ} = \int_{\Omega_X} \rho^0 \hat{\boldsymbol{\psi}}_I \hat{\boldsymbol{\psi}}_J \mathbf{I} \, d\Omega \quad (5.1)$$

The row-sum mass matrix $\hat{\mathbf{M}}^{\text{row-sum}}$ is obtained by

$$\hat{\mathbf{M}}^{\text{row-sum}} = \begin{bmatrix} \sum_{k=1}^{NP} \hat{\mathbf{M}}_{1k} & & & \mathbf{0} \\ & \sum_{k=1}^{NP} \hat{\mathbf{M}}_{2k} & & \\ & & \ddots & \\ \mathbf{0} & & & \sum_{k=1}^{NP} \hat{\mathbf{M}}_{NPk} \end{bmatrix} \quad (5.2)$$

where

$$\sum_{k=1}^{NP} \hat{\mathbf{M}}_{ik} = \sum_{k=1}^{NP} \int_{\Omega_X} \rho^0 \hat{\boldsymbol{\psi}}_i \hat{\boldsymbol{\psi}}_k \mathbf{I} \, d\Omega = \int_{\Omega_X} \rho^0 \hat{\boldsymbol{\psi}}_i \left(\sum_{k=1}^{NP} \hat{\boldsymbol{\psi}}_k \right) \mathbf{I} \, d\Omega \quad (5.3)$$

We shall examine whether the modified RKPM shape functions $\hat{\boldsymbol{\psi}}_i(\mathbf{X})$ satisfy the consistency condition. First consider the consistency condition in the RKPM shape functions to yield:

$$\sum_{k=1}^{NP} \Psi_k(X) = 1 \quad (5.4)$$

Since Eq. (5.4) holds for any $X \in \Omega_X$, the following condition can be obtained:

$$\sum_{k=1}^{NP} L_{ij} = \sum_{i=1}^{NP} \Psi_i(X_j) = 1 \quad (5.5)$$

For convenient tensor operation, we define a vector $\mathbf{1}$ as

$$\mathbf{1}^T = [1, 1, \dots, 1] \quad (5.6)$$

and Eq. (5.5) can be written in a tensor form by

$$1_i L_{ij} = 1_i \Psi_i(X_j) = 1_j \quad (5.7)$$

Using the consistency condition and the property of L in Eq. (5.7), one can further show the consistency condition in $\hat{\Psi}_i(X)$ by

$$\begin{aligned} 1 &= 1_i \Psi_i(X) = 1_i L_{ij} \hat{\Psi}_j(X) = 1_j \hat{\Psi}_j(X) \\ &= \sum_{i=1}^{NP} \hat{\Psi}_i(X) \end{aligned} \quad (5.8)$$

The row-sum mass matrix in the nodal coordinate can therefore be simplified to the following form:

$$\hat{M}^{\text{row-sum}} = \begin{bmatrix} \int_{\Omega_X} \rho^0 \hat{\Psi}_1 I \, d\Omega & & & \mathbf{0} \\ & \int_{\Omega_X} \rho^0 \hat{\Psi}_2 I \, d\Omega & & \\ & & \ddots & \\ \mathbf{0} & & & \int_{\Omega_X} \rho^0 \hat{\Psi}_n I \, d\Omega \end{bmatrix} \quad (5.9)$$

We do not integrate the diagonal terms using $\hat{\Psi}_i$ directly since $\hat{\Psi}_i$ does not have compact support. In numerical implementation, the row-sum matrix of M is first formed using the property given in Eq. (5.4):

$$M^{\text{row-sum}} = \begin{bmatrix} \int_{\Omega_X} \rho^0 \Psi_1 I \, d\Omega & & & \mathbf{0} \\ & \int_{\Omega_X} \rho^0 \Psi_2 I \, d\Omega & & \\ & & \ddots & \\ \mathbf{0} & & & \int_{\Omega_X} \rho^0 \Psi_n I \, d\Omega \end{bmatrix} \quad (5.10)$$

Define a vector η containing the diagonal terms of $M^{\text{row-sum}}$ and let $\hat{\eta}$ be the nodal coordinate counterpart of η , i.e.

$$\eta_i = M_{ii}^{\text{row-sum}} \quad \text{for } i = 1, NP \quad (\text{no sum on } i) \quad (5.11)$$

and

$$\hat{\eta} = A^{-1} \eta \quad (5.12)$$

The diagonal terms of $\hat{\mathbf{M}}^{\text{row-sum}}$ are then computed by

$$\hat{M}_{ii}^{\text{row-sum}} = \hat{\eta}_i \quad \text{for } i = 1, NP \quad (\text{no sum on } i) \quad (5.13)$$

6. Numerical examples

In hyperelastic problems 1–3, distortional-dilatational decoupled strain energy density function with reduced invariants discussed in Appendix A is used. The J_2 yield condition with associated flow rule described in Appendix B is used for elasto-plastic examples 4–6. A cubic spline kernel function is employed in RKPM computation, with a rectangular support defined using the following measure of the dilation parameter

$$r_i = \frac{a_i}{2\bar{d}_i} \quad (6.1)$$

where a_i , r_i and \bar{d}_i are the dilation parameter, the normalized dilation parameter, and the average particle distance in i th direction, respectively.

6.1. Rubber beam under pure bending deformation

The problem is taken from [26] where a cantilever beam of dimension $20 \text{ dm} \times 1 \text{ dm}$ ($1 \text{ dm} = 0.1 \text{ m}$) is subjected to an end moment by applying linear normal traction with zero resultant normal force, on the free end of the beam. This beam is made of Mooney–Rivlin material with material constants given by $A_{10} = 0.1835 \text{ MPa}$, $A_{01} = 0.0146 \text{ MPa}$ and $k = 10^3 \text{ MPa}$. The maximum tip moment of $M = 500.0 \text{ N-dm}$ is applied to the beam. To generate pure bending deformation, the appropriate boundary conditions should be prescribed on the other end of the beam, i.e. the beam is free to deform in the transverse direction and therefore only the center node is completely fixed. Also note that the linear normal traction moves with the beam so that it is tangent to the neutral surface as shown in Fig. 3. As described in Fig. 3, this problem is analyzed by RKPM and 9-node FE Lagrangian elements with pressure projected onto a linear field [27].

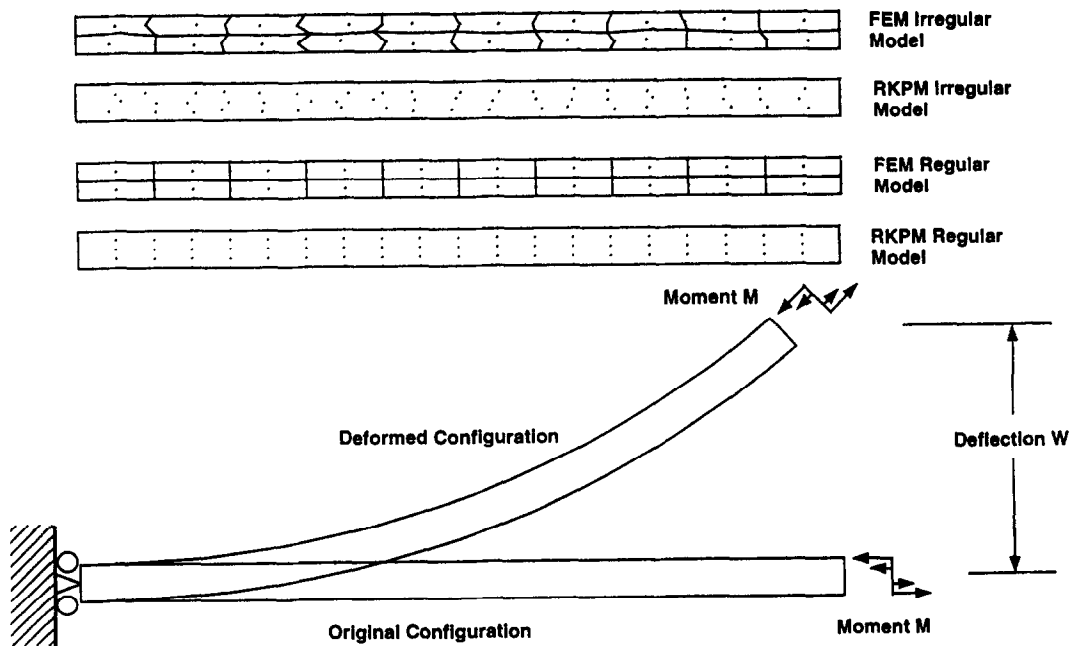


Fig. 3. Pure bending of rubber beam: problem description.

The problem is first analyzed using regularly spaced particles. An integration order of 4×4 is used in each integration zone. The effect on the particle refinement in beam thickness is studied in Fig. 4(a). The results indicate that the particle refinement in thickness of the beam is critical to solution accuracy. The model with only three particles in thickness direction produces good results in the linear range, but behaves much stiffer in large deformation.

The effect of dilation parameter is studied in Fig. 4(b) in which 20 and 4 integration zones are used in axial and thickness directions, respectively. When a small dilation parameter is used, such as the one that covers 5 particles in the thickness direction, the response is very stiff even at a linear range which leads to a large energy error. The energy error due to stiff response can be reduced simply by using larger dilation parameters in the thickness direction as shown in Fig. 4(b). The results indicate that a normalized dilation parameter in the thickness direction $r \geq 2.8$ is required in this bending problem.

Fig. 4(c) demonstrates the effects of integration order and dilation parameter. Results indicate that reduced integration improves the accuracy of the solution. However, one can also learn from Fig. 4(c) that without the appropriate use of the dilation parameter, the improvement of solution accuracy using reduced integration is marginal.

The comparison of RKPM and FEM with regular and irregular meshes is presented in Fig. 4(d). The finite element projection method using 9-node Lagrange element with pressure projected onto a linear field [27] does not have a locking or pressure oscillation problem according to the BB condition. Two 9-node finite element meshes are generated from the regularly spaced and irregularly spaced particle

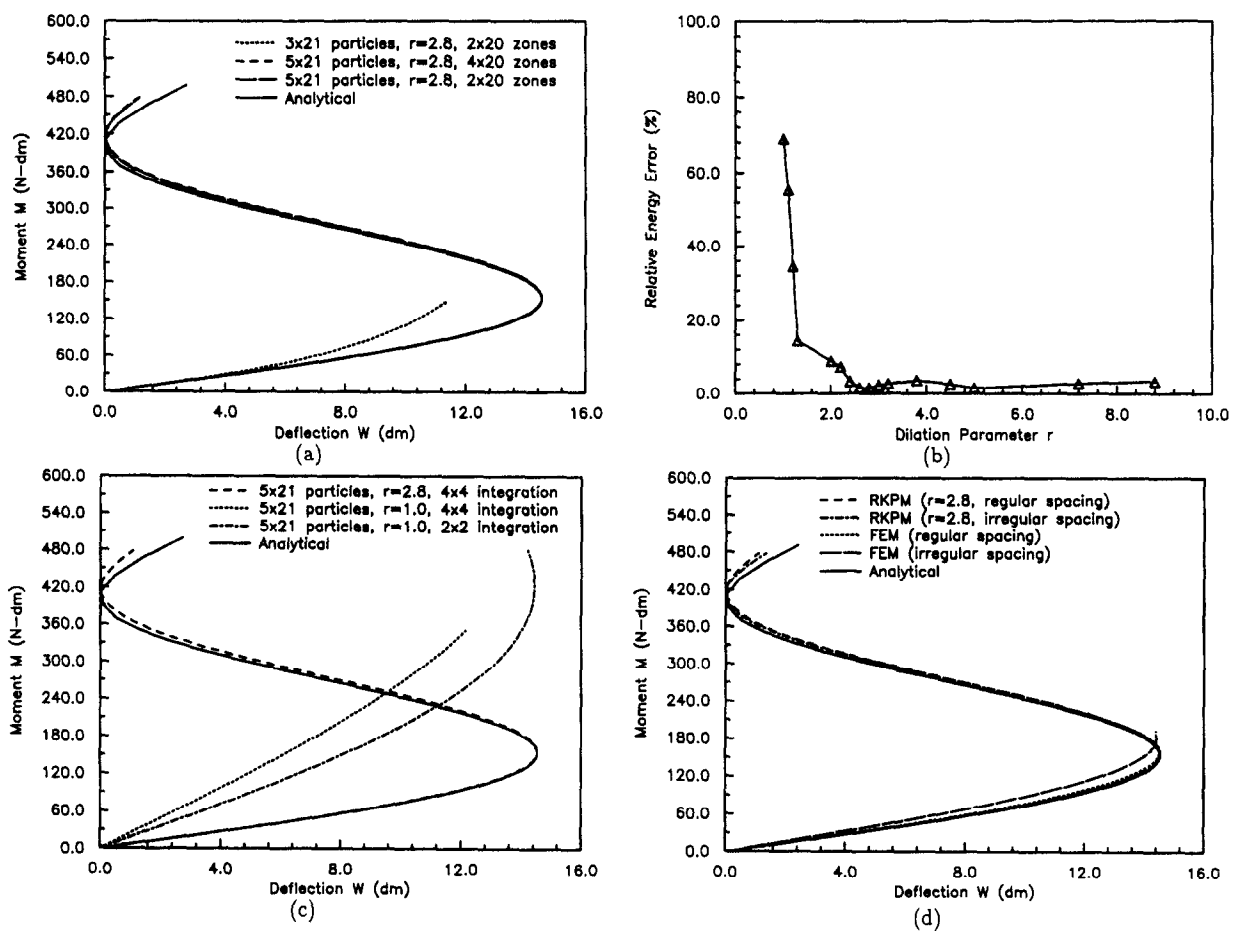


Fig. 4. Pure bending of rubber beam: (a) effect of particle refinement and integration zones in thickness direction; (b) relative energy error vs. dilation parameter at $M = 100$ N-dm; (c) effect of integration orders; (d) regular and irregular spacing models and comparison with FEM.

models. The same load step size and convergence criteria as those used in the RKPM calculation are used for finite element computation. The finite element calculations diverge at $M = 198.2$ N-dm using irregular mesh and at $M = 226.8$ N-dm using regular mesh. Further, the accuracy of finite element solution is lower than RKPM. Table 2 compares the RKPM and finite element deflection solutions at $M = 125$ N-dm. The RKPM performs better than FEM, particularly when an irregular mesh is used.

With the RKPM method, the beam can be bent to a very large deformation without experiencing a divergence problem, and yet produces accurate results as shown in Fig. 4(d). The bending deformed geometries of regular particle and irregular particle models at a maximum moment of 500.0 N-dm are shown in Fig. 5.

6.2. Bonded rubber deformation—an application to rubber bearing

In bearing applications, rubber pads are sandwiched between metal layers. The rubber–metal bonding provides high interlaminar stiffness and low shear stiffness. The detailed physical significance and numerical studies of this problem were discussed in [27]. This example studies the rubber deformations that usually exist in bearing applications. The rubber properties are $A_{10} = 0.373$ MPa, $A_{20} = -0.031$ MPa, $A_{30} = 0.005$ MPa and $k = 10^5$ MPa. In the following analyses, 5×4 integration zone with 5×5 integration order are used and normalized dilation parameters are taken to be $r_x = r_y = 1.0$.

A plane-strain rubber pad, with a width-to-thickness ratio of 10:1, is first sheared while holding constant distance between the two metal plates. Perfect bonding between rubber–metal interfaces is assumed and metal plates are treated as rigid bodies; therefore, only the rubber is modeled by regularly spaced and irregularly spaced particles. The predicted shear load–deflection curve is compared with the simple shear solution in Fig. 6(a).

The bulk behavior of rubber is studied through the analysis of apparent Young's modulus in bonded rubber components subjected to an interlaminar compression. Plane-strain rubber components with thickness-to-height ratio (w/h) varying from 10^{-2} to 10^3 are considered in the analysis to study the effect of the shape factor on apparent Young's modulus in bonded rubber. In this study, the bulk modulus effect is also investigated and $k = 10^3, 10^4, 10^5$ MPa are used in the analysis for comparison. The RKPM results obtained from an irregularly spaced particle model are compared against Gent's approximation [28] in Fig. 6(b) and the agreement is satisfactory. Results also show that RKPM accurately captures rubber bulk behavior.

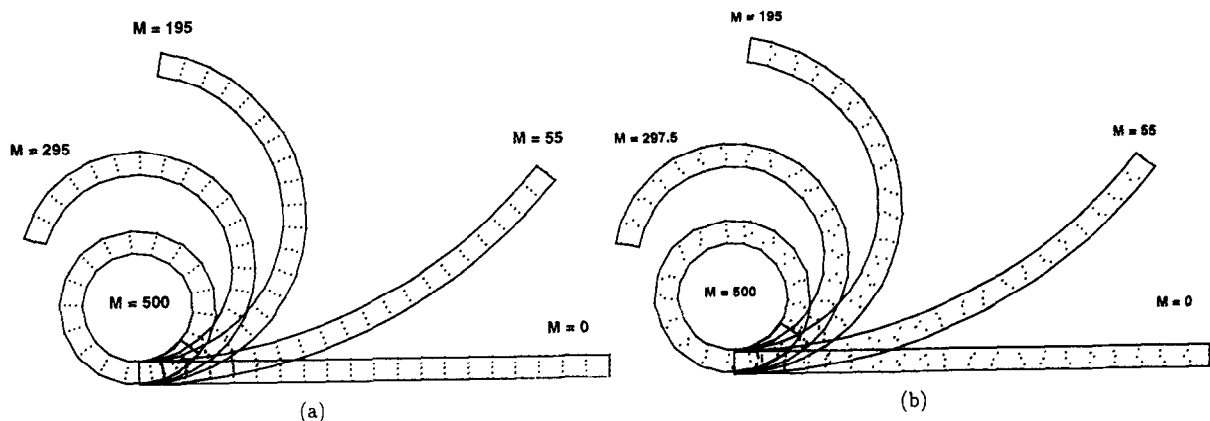


Fig. 5. Rubber beam deformation under pure bending: (a) regular spacing model; (b) irregular spacing model.

Table 2
Comparison of RKPM and FEM deflections in bending problem at $M = 125$ N-dm

Analytical	RKPM (regular)	RKPM (irregular)	FEM (regular)	FEM (irregular)
1.392 dm	1.391 dm	1.382 dm	1.320 dm	1.226 dm

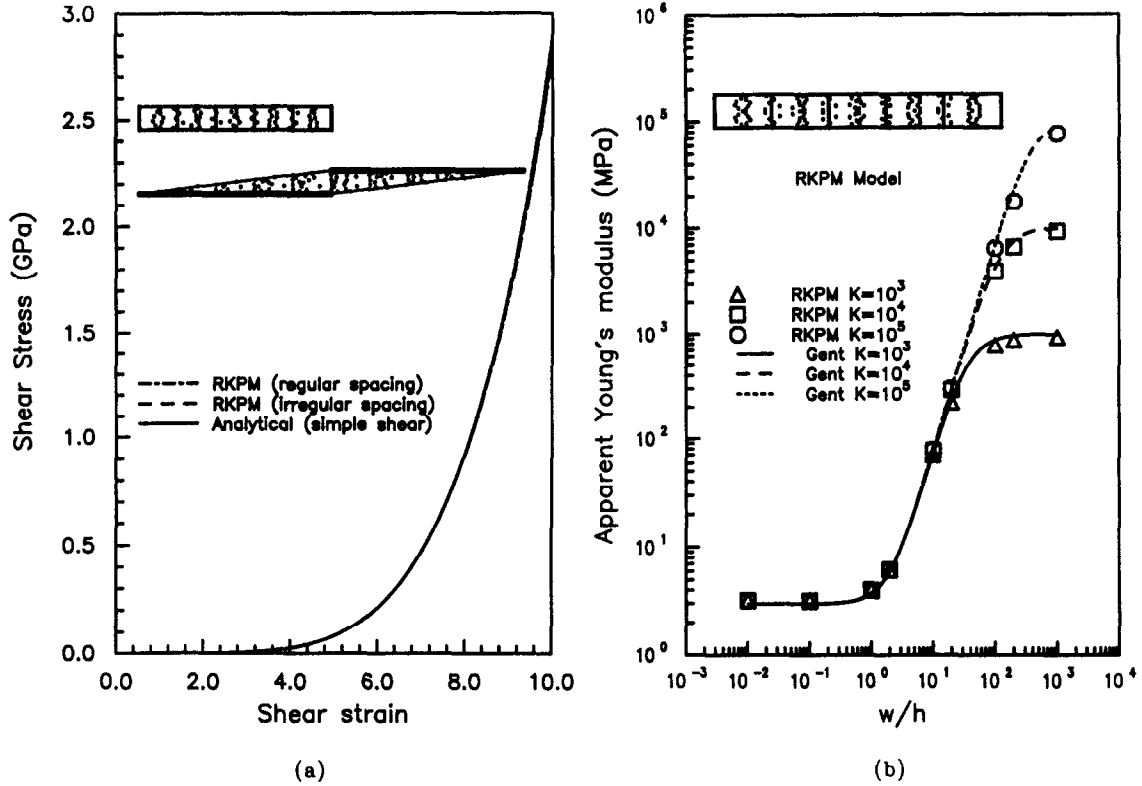


Fig. 6. Analysis of a rubber bearing using RKPM: (a) shape factor effect of bonded rubber; (b) bonded rubber under shear.

The finite element simulation of bonded rubber subjected to large interlaminar deformation usually failed due to excessive mesh distortion occurring near the edges on the rubber–metal interfaces [27]. A plane-strain bonded rubber with diameter to thickness ratio of 10 is analyzed herein. With finite element analysis fails at 21% in compression and 500% in tension, RKPM analysis advances further without experiencing mesh distortion difficulty as shown in Fig. 7.

6.3. Analysis of engine mount

In this problem, the deformation of an engine mount due to vertical static load is analyzed using a finite element method and RKPM. The non-linear rubber behavior is described by a Mooney–Rivlin strain energy density function with material constants $A_{10} = 0.145$ MPa, $A_{01} = 0.062$ MPa, and $k = 6.9 \times 10^3$ MPa taken from [29]. In the finite element analysis, only the rubber components are modeled by a finite element mesh shown in Fig. 8. The center metal piece, treated as a rigid body, is connected to the engine and is forced to move downward in a vertical direction. The outer surface of the engine mount is bonded to a metal casing that is attached to the car body and therefore the outer surface of the analysis model is completely fixed. The finite element analysis is terminated due to severe mesh distortion near the lower corners of the lower rubber legs as shown in Fig. 8, and a mesh refinement in the highly deformed areas is needed.

A particle model using the existing nodes in finite element model is first generated to analyze the same problem. The existing mesh in the finite element model is taken as integration zones in RKPM computation. The normalized dilation parameters of $r_s = r_y = 1.0$ are used. Knowing that a localized distortion occurs near the lower corners of rubber legs, a refined RKPM model is generated simply by adding more nodes near the highly deformed areas (see Fig. 8). With this refinement, the analysis is completed without mesh distortion problem as shown in Fig. 8. This example demonstrates the convenience of model refinement using RKPM.

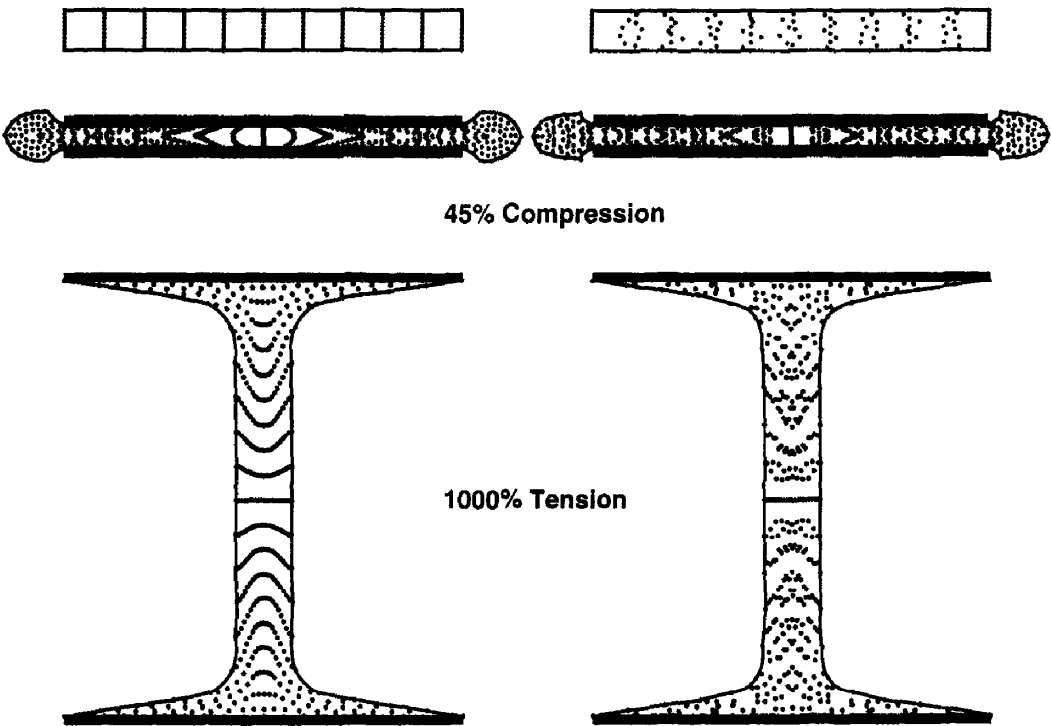


Fig. 7. Deformation of bonded rubber under tension and compression.

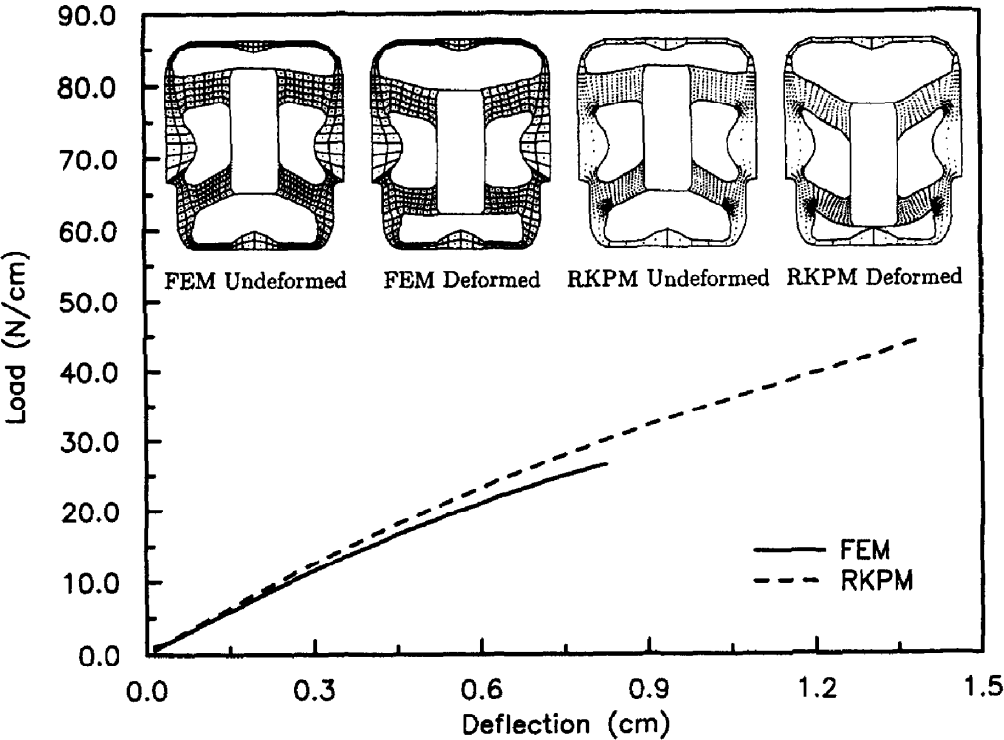


Fig. 8. Engine mount: comparison of load–deflection curves of FEM and RKPM.

6.4. Plane-strain elasto-plastic cylinder subjected to internal pressure

This benchmark problem is taken from [30]. The tube is assumed to be infinitely long in the longitudinal direction, and the inner and outer radii of the tube are 100 cm and 200 cm, respectively. The tube is made of perfect plastic material with material properties: Young's modulus $E = 207\,000\text{ N/mm}^2$, Poisson's ratio $\nu = 0.3$, yield stress $k = 207.9\text{ N/mm}^2$. As shown in Fig. 9(a), only one section of the tube is modeled by axisymmetric particles, and proper constraints are imposed in the longitudinal direction to reflect plane-strain condition.

In RKPM computation, 4×1 integration zones with 2×2 quadrature rule are used. In this problem constant dilation parameters are assigned to every node based on $r_x = 1.2$ and $r_y = 1.5$ in radial and longitudinal directions, respectively. The RKPM results are compared with the results of an 8-node isoparametric axisymmetric element with 2×2 integration reported in [30]. The comparison of radial and circumferential stress distributions are shown in Figs. 9(a) and 9(b), respectively, with satisfactory agreement.

6.5. Aluminum bar impact on a rigid wall

This is a classical impact problem introduced by Taylor [31] to measure yield properties. Wilkins et al. [32] later performed a complementary experimental and computational study for Taylor cylinder impact problem. The initial radius and initial height of the aluminum bar are 0.391 cm and 2.346 cm, respectively. The material properties of the cylinder are: initial density $\rho_0 = 2700\text{ kg/m}^3$, Young's modulus $E = 78.2\text{ GPa}$, Poisson's ratio $\nu = 0.3$, and J_2 plasticity with initial yield stress $Y = 0.29\text{ GPa}$. The initial impact velocity is 373 m/s and the rigid surface is assumed to be frictionless.

Explicit time integration method with row-sum mass matrix given in Eq. (5.13) is employed. The first analysis considers a perfect plastic material. The computation proceeds until the plastic deformation is fully developed. Two particle models are used in RKPM calculation, one with 6×31 particles and the other with 11×31 particles for half of the structure. The coarse particle model has 5 radial zones and 30 axial zones, whereas the fine particle model has 10 radial zones and 30 axial zones. Normalized dilation parameters of $r_x = r_y = 1.0$ are used in the material kernel function and the current approach requires no readjustment of dilation parameters under large deformation. The final deformed geometries are characterized by the measure of deformed height and deformed radius near the rigid surface. The RKPM results are compared with finite element predictions using HEMP [32], CSQ

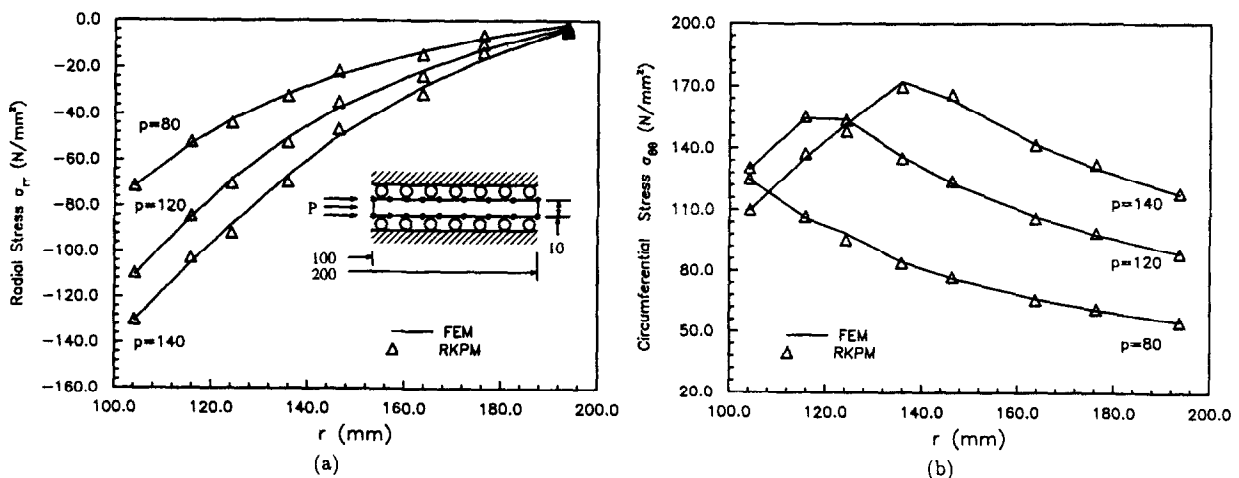


Fig. 9. Long cylindrical tube subjected to internal pressure: (a) radial stress distribution at various pressure intensities; (b) circumferential stress distributions at various pressure intensities.

reported in Predebon et al. [33], and particle in cell solution using FLIP [34] in Table 3. The final deformed geometries for a perfect plastic case are plotted in Fig. 10 using coarse and fine particles.

The second analysis deals with strain-hardening elasto-plasticity with hardening rules given by

$$H(\bar{\epsilon}^p) = 0, \quad (6.2)$$

$$K(\bar{\epsilon}^p) = Y(1 + 125\bar{\epsilon}^p)^{0.1} \quad (6.3)$$

where $\bar{\epsilon}^p$ is the effective plastic strain and H and K are the plastic modulus and yield stress defined in Appendix B, respectively. The experimentally measured deformed height is 1.651 cm, whereas RKPM predicts 1.644 cm and 1.645 cm using coarse and fine particle models, respectively. The experimental data of the deformed radius near rigid surface is not available and therefore comparison with other numerical solutions [32–34] are made in Table 4. The final deformed geometries of strain-hardening analysis are plotted in Fig. 10 using coarse and fine particles, respectively. The effective plastic strain contour plots for both perfect plastic and strain-hardening materials are presented in Fig. 11, and the distributions for both cases agrees with the finite element Lagrangian results reported in [32].

Table 3

Comparison of deformed geometries for perfect plastic case of bar impact problem

	HEMP	CSQ	CSQ-fine	FLIP	RKPM	RKPM-fine
Height (cm)	1.479	1.477	1.433	1.45	1.448	1.454
Radius (cm)	0.898	0.826	0.935	0.98	1.039	1.051

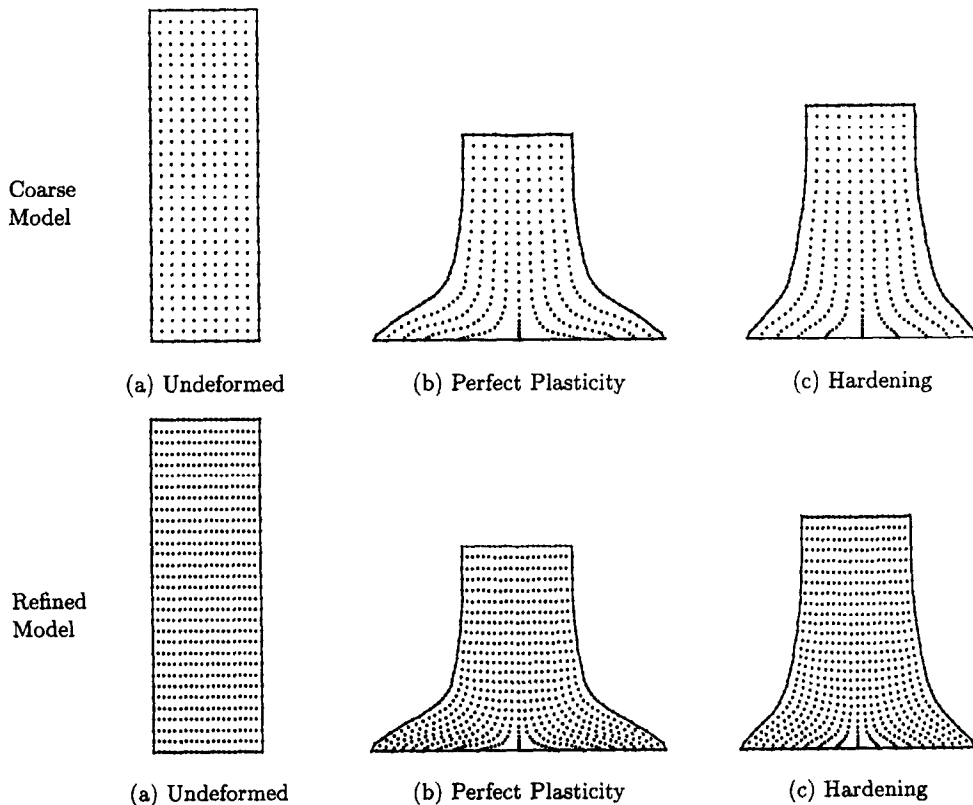


Fig. 10. Cylinder impact deformations predicted by RKPM.

Table 4

Comparison of deformed geometries for strain hardening case of bar impact problem

	HEMP	CSQ	CSQ-fine	FLIP	RKPM	RKPM-fine
Height (cm)	1.652	1.605	1.584	1.65	1.644	1.645
Radius (cm)	0.742	0.720	0.795	0.78	0.827	0.837

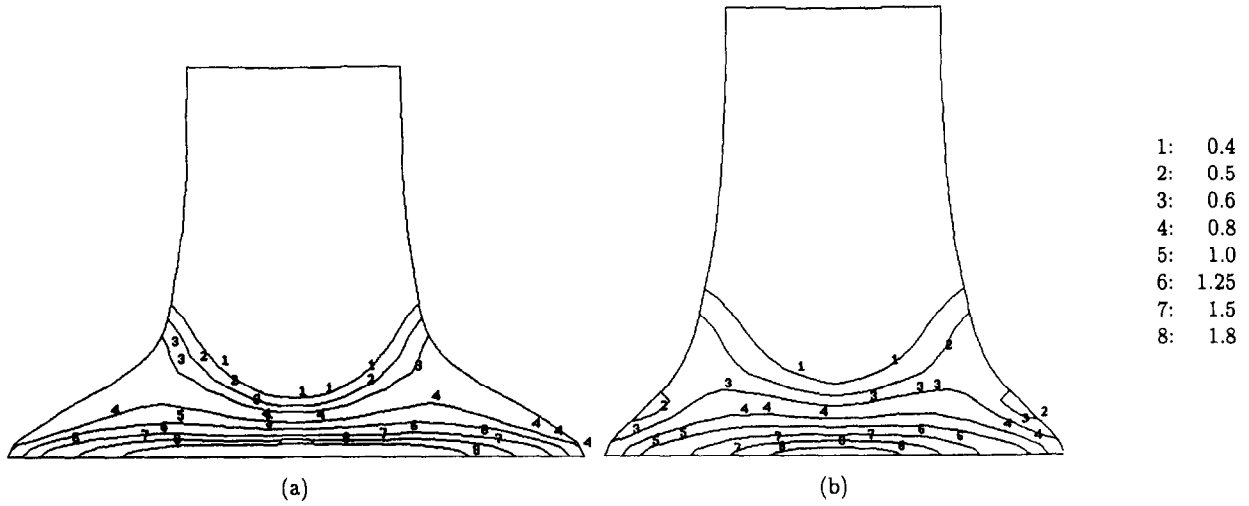


Fig. 11. Effective plastic strain contour of impact cylinder: (a) perfect plasticity; (b) hardening.

6.6. Necking of a circular bar

An axisymmetric bar with 53.334 mm in length and 6.413 mm in radius is subjected to an axial prescribed displacement as shown in Fig. 12(a). The two ends of the bar are totally constrained to reflect the actual experimental test fixture [35] and only one quarter of the specimen is modeled by axisymmetric RKPM particles with proper symmetric boundary conditions specified. To simulate necking, a geometric imperfection is introduced by a linear reduction in radius along the length, with radius at the center to be 98.2% of the radius at the end. The problem is analyzed by a displacement controlled method. The material properties are: Young's modulus $E = 206.9$ GPa, Poisson's ratio $\nu = 0.29$, and an isotropic hardening rule is given by

$$K(\bar{\epsilon}^p) = \sigma_Y + \alpha \bar{\epsilon}^p + (\sigma_Y^\infty - \sigma_Y)(1 - e^{-\beta \bar{\epsilon}^p}) \quad (6.4)$$

where K and $\bar{\epsilon}^p$ are the yield stress and effective plastic strain, respectively, defined in Appendix B, and $\sigma_Y = 0.45$ GPa, $\sigma_Y^\infty = 0.715$ GPa, $\alpha = 0.12924$ GPa, $\beta = 16.93$.

Two particle models as shown in Fig. 12(a) are used in this problem. Constant dilation parameters are assigned to every node based on $r_x = 1.6$ and $r_y = 1.0$ in longitudinal and transverse directions, respectively. Note that larger normalized dilation parameter in the longitudinal direction is used due to the high nodal spacing irregularity in that direction. The analysis proceeds until the total axial displacement reaches 14 mm (7 mm for half model). The deformed geometries are plotted in Fig. 12(a) and the predicted necking behavior and load–displacement response are compared favorably with experimental data [35] in Figs. 12(b)–(d).

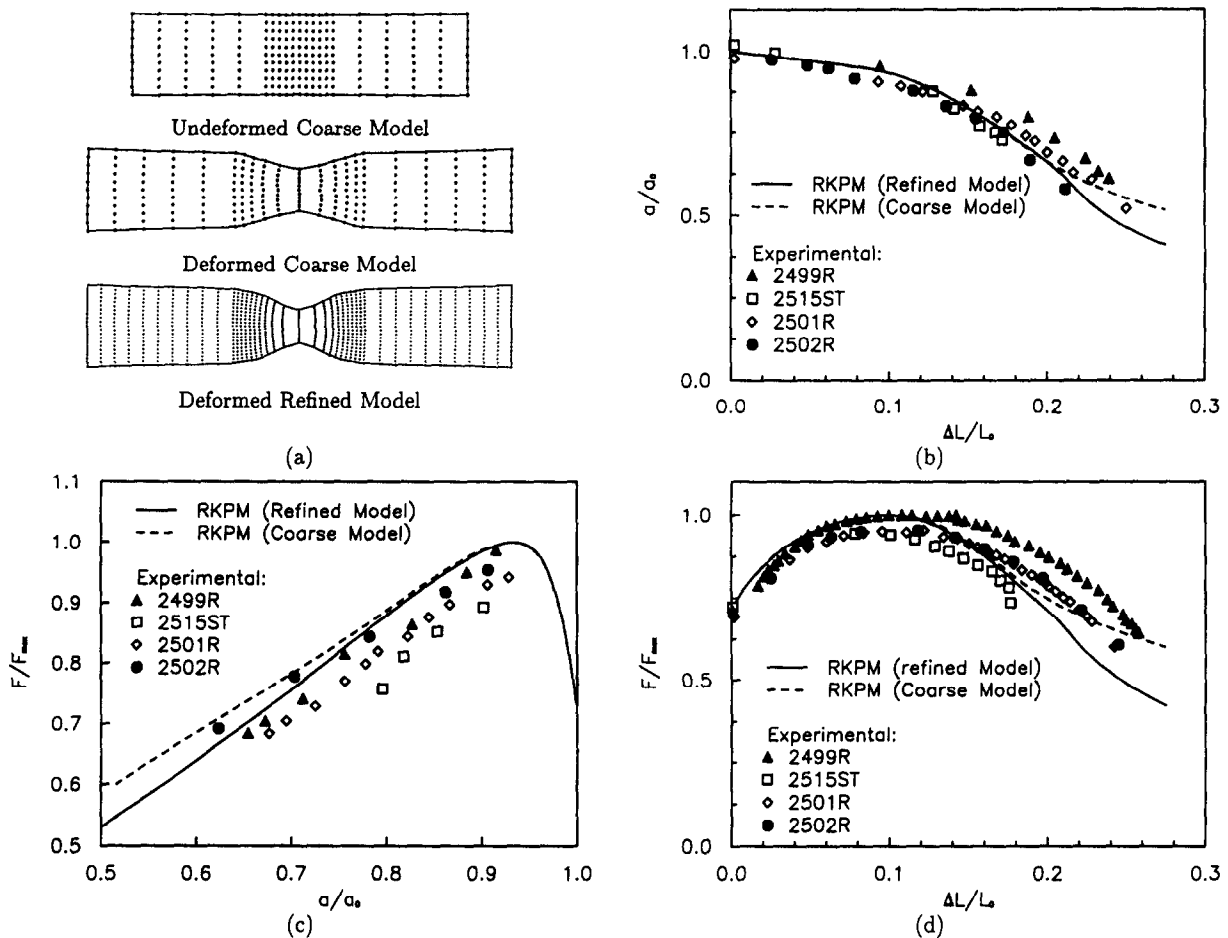


Fig. 12. Analysis of circular bar necking using RKPM: (a) undeformed and deformed geometries; (b) normalized neck radius a/a_0 versus strain $\Delta L/L_0$ for gauge of length $L_0 = 50.8$ mm; (c) normalized load F/F_{max} versus normalized neck radius a/a_0 ; (d) normalized load F/F_{max} versus strain $\Delta L/L_0$ gauge of length $L_0 = 50.8$ mm.

7. Conclusion

This paper addresses issues associated with the extension of RKPM to large deformation analysis. To be able to apply RKPM to non-linear elastic and inelastic structures, both path-independent and path-dependent materials are considered in the formulation. The development in this paper features the following: (1) the consistent numerical integration of the moment matrix and its derivative is discussed, (2) a transformation method to exactly impose essential boundary conditions is proposed, (3) a material RKPM shape function is proposed so that the stability conditions are satisfied throughout large deformation, (4) the use of material shape function also enhances efficiency for the calculation of the transformation matrix, and (5) the construction of lumped mass at nodal coordinate is used for explicit time integration.

In this paper, the integration method for moment matrix and its derivative is first studied. Since the RKPM shape function is obtained from the discretization of the reproducing equation, the moment matrix and its derivatives need to be integrated using the same discretization method employed in the reproducing equation so that the reproducing conditions are retained in the discretized reproducing equation.

In this implementation, a method that transforms the unknown variables from generalized coordinate to nodal coordinate is introduced to allow a direct imposition of essential boundary conditions. This method could be versatile in linear analysis since a transformation matrix needs to be formed and the

computation also requires the inverse of the transformation matrix. Nevertheless, in large deformation analysis, these additional efforts pay off only at the initial stage because the transformation matrix is reusable at each incremental step. This efficiency is achieved by the use of material kernel function and shape function. This method is more attractive than the Lagrange multiplier method, since the Lagrange multipliers need to be solved at each incremental step.

Indeed, the use of material kernel function also assures stability of RKPM large deformation analysis. As discussed in [17,18,21], the RKPM stability requires that the support of kernel function covers enough particles. One can define the kernel function in the initial configuration that satisfies stability conditions; however, the stability conditions are not guaranteed when materials deform in large scale if the kernel function has fixed support size in space. In this approach, the kernel function and basis functions are constructed at the material coordinate. The material kernel function and consequently the RKPM material shape function deform with material particles and the supports cover the same set of nodes throughout structural deformation. With this implementation, the stability conditions are satisfied once and for all.

To adopt Galerkin approximation using RKPM material shape function, both hyperelasticity and elasto-plasticity variational equations are formulated with reference to initial configuration. In elasto-plasticity, the calculation of velocity gradient is required for Cauchy stress update. A chain rule in conjunction with the inverse of deformation gradient are used to avoid taking spatial derivatives of a material shape function. In this paper, a row-sum lumped mass matrix at nodal coordinate is also implemented for use in conjunction with the explicit time integration method.

The numerical examples presented in this paper show good performance in using RKPM for large deformation analysis. High solution accuracy is observed in both hyperelasticity and elasto-plasticity problems. Compared to the finite element method, RKPM can better handle large deformation without any special numerical treatment due to the use of smooth material kernel function. The numerical results also show the absence of volumetric locking in dealing with (nearly) incompressible materials under large deformation. The effectiveness of the method to handle excessive material distortion is demonstrated in bending, necking and impact problems, as well as in bearing and engine mount applications.

Acknowledgment

The support of this research by Army TARDEC to the University of Iowa and Office of Naval Research to Northwestern University is greatly acknowledged.

Appendix A. Second Piola–Kirchhoff stress and material response tensors for hyperelasticity

A strain energy density function that decouples the distortional and dilatational deformation [36,27] is

$$W(\bar{I}_1, \bar{I}_2, J) = \bar{W}(\bar{I}_1, \bar{I}_2) + \tilde{W}(J) \quad (\text{A.1})$$

where $\bar{W}(\bar{I}_1, \bar{I}_2)$ and $\tilde{W}(J)$ are the distortional and dilatational strain energy density functions given by

$$\bar{W}(\bar{I}_1, \bar{I}_2) = \sum_{m+n=1}^{\infty} A_{mn} (\bar{I}_1 - 3)^m (\bar{I}_2 - 3)^n \quad (\text{A.2})$$

$$\tilde{W}(J) = \frac{k}{2} (J - 1)^2 \quad (\text{A.3})$$

where \bar{I}_1 and \bar{I}_2 are the reduced invariants proposed by Penn [37] to separate the distortional and dilatational deformation:

$$\bar{I}_1 = I_1 I_3^{-1/3}, \quad (\text{A.4})$$

$$\bar{I}_2 = I_2 I_3^{-2/3}, \quad (\text{A.5})$$

and I_1, I_2, I_3 are the first, second and third invariants of Green deformation tensor G , respectively, $J = I_3^{1/2}$ and k is the bulk modulus to be measured experimentally. It can be shown that the hydrostatic pressure, defined as one third of the trace of Cauchy stress, can be related to $\tilde{W}(J)$ by

$$P = \sigma_{mm}/3 = \frac{\partial \tilde{W}}{\partial J}; \quad m = 1, 2, 3 \quad (\text{A.6})$$

where σ_{ij} is the Cauchy stress. The second Piola–Kirchhoff stress calculated from the strain energy density function (Eq. (3.7)) is

$$S_{ij} = 2 \left[q_1 I_3^{-1/3} \left(\delta_{ij} - \frac{1}{3} I_1 G_{ij}^{-1} \right) + q_2 I_3^{-2/3} \left(I_1 \delta_{ij} - G_{ij} - \frac{2}{3} I_2 G_{ij}^{-1} \right) \right] + P J G_{ij}^{-1} \quad (\text{A.7})$$

where

$$q_n = \frac{\partial \tilde{W}}{\partial \bar{I}_n}, \quad n = 1, 2 \quad (\text{A.8})$$

Similarly, the material response tensor is obtained according to Eq. (3.28a) to yield

$$C_{ijkl} = \frac{\partial^2 W}{\partial E_{ij} \partial E_{kl}} = \bar{C}_{ijkl} + \tilde{C}_{ijkl} \quad (\text{A.9})$$

The explicit expressions of \bar{C}_{ijkl} and \tilde{C}_{ijkl} are given by

$$\begin{aligned} \bar{C}_{ijkl} &= \frac{\partial^2 \tilde{W}}{\partial E_{ij} \partial E_{kl}} \\ &= \frac{2}{3} q_1 I_3^{-1/3} \left\{ -2(\delta_{ij} G_{kl}^{-1} + \delta_{kl} G_{ij}^{-1}) + \frac{1}{3} I_1 [2G_{ij}^{-1} G_{kl}^{-1} + 3(G_{ik}^{-1} G_{jl}^{-1} + G_{il}^{-1} G_{jk}^{-1})] \right\} \\ &\quad + \frac{4}{3} q_2 I_3^{-2/3} \left\{ -2I_1 (\delta_{ij} G_{kl}^{-1} + \delta_{kl} G_{ij}^{-1}) + 2(G_{ik}^{-1} G_{jl}^{-1} + G_{il}^{-1} G_{jk}^{-1}) \right. \\ &\quad \left. + I_2 \left(\frac{4}{3} G_{ij}^{-1} G_{kl}^{-1} + G_{ik}^{-1} G_{jl}^{-1} + G_{il}^{-1} G_{kj}^{-1} \right) + \frac{3}{2} [2\delta_{ij} \delta_{kl} - (\delta_{ik} \delta_{jl} + \delta_{il} \delta_{kj})] \right\} \\ &\quad + 4t_{11} I_3^{-2/3} \left(\delta_{ij} - \frac{1}{3} I_1 G_{ij}^{-1} \right) \left(\delta_{kl} - \frac{1}{3} I_1 G_{kl}^{-1} \right) + 4t_{12} I_3^{-1} \left[\left(\delta_{ij} - \frac{1}{3} I_1 G_{ij}^{-1} \right) \left(I_1 \delta_{kl} - G_{kl} \right. \right. \\ &\quad \left. \left. - \frac{2}{3} I_2 G_{kl}^{-1} \right) \right] + 4t_{22} I_3^{-4/3} \left(I_1 \delta_{ij} - G_{ij} - \frac{2}{3} I_2 G_{ij}^{-1} \right) \left(I_1 \delta_{kl} - G_{kl} - \frac{2}{3} I_2 G_{kl}^{-1} \right), \end{aligned} \quad (\text{A.10})$$

$$\tilde{C}_{ijkl} = kJ(J-1)(G_{ij}^{-1} G_{kl}^{-1} - G_{ik}^{-1} G_{jl}^{-1} - G_{il}^{-1} G_{jk}^{-1}) + kJ^2 G_{ij}^{-1} G_{kl}^{-1} \quad (\text{A.11})$$

where

$$t_{ij} = \frac{\partial^2 W}{\partial \bar{I}_i \partial \bar{I}_j} \quad (\text{A.12})$$

Appendix B. Cauchy stress update and consistent tangent for elastoplasticity

The Jaumann stress rate given in Eq. (3.9) will be integrated using an incrementally objective algorithm proposed by Hughes and Wignot [38]. At the time step of $n+1$, the elastic trial of Cauchy stress τ , back stress α and yield radius K are calculated by

$$\boldsymbol{\tau}_{n+1}^{\text{tr}} = \boldsymbol{Q}_{n+1/2} \boldsymbol{\tau}_n \boldsymbol{Q}_{n+1/2}^T + \boldsymbol{C}^e \Delta \boldsymbol{\varepsilon}_{n+1/2} \quad (\text{B.1})$$

$$\boldsymbol{\alpha}_{n+1}^{\text{tr}} = \boldsymbol{Q}_{n+1/2} \boldsymbol{\alpha}_n \boldsymbol{Q}_{n+1/2}^T \quad (\text{B.2})$$

$$K_{n+1}^{\text{tr}} = K_n \quad (\text{B.3})$$

where the orthogonal matrix $\boldsymbol{Q}_{n+1/2}$ and strain increment $\Delta \boldsymbol{\varepsilon}_{n+1/2}$ are defined by

$$\boldsymbol{Q}_{n+1/2} = \boldsymbol{I} + \left(\boldsymbol{I} - \frac{1}{2} \boldsymbol{W}_{n+1/2} \right)^{-1} \boldsymbol{W}_{n+1/2} \quad (\text{B.4})$$

$$(\boldsymbol{W}_{ij})_{n+1/2} = \frac{1}{2} \left[\frac{\partial \Delta u_i}{\partial (x_j)_{n+1/2}} - \frac{\partial \Delta u_j}{\partial (x_i)_{n+1/2}} \right] \quad (\text{B.5})$$

$$(\Delta \boldsymbol{\varepsilon}_{ij})_{n+1/2} = \frac{1}{2} \left[\frac{\partial \Delta u_i}{\partial (x_j)_{n+1/2}} + \frac{\partial \Delta u_j}{\partial (x_i)_{n+1/2}} \right] \quad (\text{B.6})$$

$$(x_i)_{n+1/2} = (x_i)_n + \frac{1}{2} \Delta u_i \quad (\text{B.7})$$

and \boldsymbol{C}^e is the elastic corotational material response tensor. In this paper, J_2 yield condition with the associate flow rule is considered in which the yield criterion is formulated as

$$f(\boldsymbol{\xi}, \boldsymbol{\alpha}, K) = \|\boldsymbol{\xi}\| - \sqrt{\frac{2}{3}} K(\bar{\varepsilon}^p) \quad (\text{B.8})$$

$$\boldsymbol{\xi} = \boldsymbol{s} - \boldsymbol{\alpha}(\bar{\varepsilon}^p) \quad (\text{B.9})$$

where \boldsymbol{s} is the deviatoric Cauchy stress and $\bar{\varepsilon}^p$ is the effective plastic strain. The hardening rules are given by

$$\dot{\boldsymbol{\alpha}} = \frac{2}{3} H(\bar{\varepsilon}^p) \dot{\bar{\varepsilon}}^p \quad (\text{B.10})$$

$$K = K(\bar{\varepsilon}^p) \quad (\text{B.11})$$

where H is the plastic modulus, and $\dot{\bar{\varepsilon}}^p$ is the plastic strain rate. If the elastic trial stress states locate outside the yield surface, the following radial return mapping produces [39] for non-linear kinematics and isotropic hardening are used to calculate the final stress states:

$$\boldsymbol{s}_{n+1} = \boldsymbol{s}_{n+1}^{\text{tr}} - \Delta \lambda (2\mu \boldsymbol{n}) \quad (\text{B.12})$$

$$\boldsymbol{\alpha}_{n+1} = \boldsymbol{\alpha}_{n+1}^{\text{tr}} + \sqrt{\frac{2}{3}} \Delta H \mu \boldsymbol{n} \quad (\text{B.13})$$

$$K_{n+1} = K(\bar{\varepsilon}_{n+1}^p) \quad (\text{B.14})$$

$$\bar{\varepsilon}_{n+1}^p = \bar{\varepsilon}_n^p + \sqrt{\frac{2}{3}} \Delta \lambda \quad (\text{B.15})$$

$$\Delta H = H(\bar{\varepsilon}_{n+1}^p) - H(\bar{\varepsilon}_n^p) \quad (\text{B.16})$$

$$\boldsymbol{n} = \boldsymbol{\xi}_{n+1}^{\text{tr}} / \|\boldsymbol{\xi}_{n+1}^{\text{tr}}\| \quad (\text{B.17})$$

$$\boldsymbol{\xi}_{n+1}^{\text{tr}} = \boldsymbol{s}_{n+1}^{\text{tr}} - \boldsymbol{\alpha}_{n+1}^{\text{tr}} \quad (\text{B.18})$$

where μ is the shear modulus, \boldsymbol{n} is the unit vector normal to the yield surface and $\Delta \lambda$ is the magnitude of the plastic strain increment that is obtained from the consistency condition. For a general non-linear hardening rule, iteration procedures are required to obtain $\Delta \lambda$.

The corotational elasto-plastic material response tensor $\boldsymbol{C}_{ijkl}^{\text{ep}}$ is formed using the consistent tangent proposed by Simo et al. [40]:

$$C_{ijkl}^{ep} = C_{ijkl}^e - 2\mu(\beta_1 I_{ijkl}^{dev} + \beta_2 n_{ij} n_{kl}) \quad (B.19)$$

$$I_{ijkl}^{dev} = \frac{1}{2}(\delta_{ik}\delta_{jl} + \delta_{il}\delta_{jk}) - \frac{1}{3}\delta_{ij}\delta_{kl} \quad (B.20)$$

$$\beta_1 = \sqrt{\frac{2}{3}} \frac{[K_{n+1} + \Delta H]}{\|\xi_{n+1}^{tr}\|} - 1 \quad (B.21)$$

$$\beta_2 = \frac{1}{1 + \frac{[K' + H]_{n+1}}{3\mu}} + \beta_1 \quad (B.22)$$

$$K' = \frac{dK(\bar{\epsilon}^p)}{d\bar{\epsilon}^p} \quad (B.23)$$

References

- [1] W.K. Liu, H. Chang, J.S. Chen and T. Belytschko, Arbitrary Lagrangian Eulerian Petrov–Galerkin finite elements for nonlinear continua, *Comput. Methods Appl. Mech. Engrg.* 68(3) (1988) 259–310.
- [2] W.K. Liu, J.S. Chen, B. Belytschko and Y.F. Zhang, Adaptive ALE finite elements with particular reference to external work rate on frictional interface, *Comput. Methods Appl. Mech. Engrg.* 93 (1991) 189–216.
- [3] L. Lucy, Numerical approach to testing the fission hypothesis, *Astron. J.* 82 (1977) 1013–1024.
- [4] R.A. Gingold and J.J. Monaghan, Smoothed particle hydrodynamics: Theory and application to non-spherical stars, *Monthly Notices Royal astron. Soc.* 181 (1977) 375–389.
- [5] J.J. Monaghan, Why particle methods work, *SIAM J. Sci. Stat. Comput.* 3(4) (1982) 422–433.
- [6] J.J. Monaghan, An introduction to SPH, *Comput. Phys. Comm.* 48 (1988) 89–96.
- [7] L.D. Liberkey, A.G. Petschek, T.C. Carney, J.R. Hipp and F.Z. Alliahdadi, High strain Lagrangian hydrodynamics, *J. Comput. Phys.* 109 (1993) 67–75.
- [8] F.H. Harlow, The particle-in-cell computing method for fluid dynamics, in: B. Adler, S. Fernbach and M. Rotengerb, eds., *Methods for Comput. Phys.* 3 (1964) 319–343.
- [9] J.U. Brackbill, FLIP: A method for adaptivity zoned, particle-in-cell calculations of fluid flows in two dimensions, *J. Comput. Phys.* 65 (1986) 314–343.
- [10] D. Sulsky, Z. Chen and H.L. Schreyer, A particle method for history-dependent materials, *Comput. Methods Appl. Mech. Engrg.* 118 (1994) 179–196.
- [11] B. Nayroles, G. Touzot and P. Villon, Generalizing the finite element method: Diffuse approximation and diffuse elements, *Comput. Mech.* 10 (1992) 307–318.
- [12] T. Belytschko, Y.Y. Lu and L. Gu, Element-free Galerkin methods, *Int. J. Numer. Methods Engrg.* 37 (1994) 229–256.
- [13] Y.Y. Lu, T. Belytschko and L. Gu, A new implementation of the element-free Galerkin method, *Comput. Methods Appl. Mech. Engrg.* 113 (1994) 397–414.
- [14] T. Belytschko, Are finite elements passé?, *USACM Bulletin* 7(3) (1994).
- [15] T. Belytschko, L. Gu and Y.Y. Lu, Fracture and crack growth by EFG method, *Model. Simul. Mater. Sci. Engrg.* 2 (1994) 519–534.
- [16] T. Belytschko, Y. Krongauz, M. Fleming, D. Organ and W.K. Liu, Smoothing and accelerated computations in the element-free Galerkin method, *J. Comput. Appl. Math.* (1995), accepted.
- [17] W.K. Liu, S. Jun, S. Li, J. Adee and T. Belytschko, Reproducing Kernel Particle Methods for structural dynamics, *Int. J. Numer. Methods Engrg.* 38 (1995) 1655–1679.
- [18] W.K. Liu, S. Jun and Y.F. Zhang, Reproducing Kernel Particle Method, *Int. J. Numer. Methods Fluids* 20 (1995) 1081–1106.
- [19] W.K. Liu, An introduction to wavelet Reproducing Kernel Particle Methods, *USACM Bull.* 8(1) (1995) 3–16.
- [20] W.K. Liu and Y.J. Chen, Wavelet and multiple scale Reproducing Kernel Methods, *Int. J. Numer. Methods Fluids* 21 (1995) 901–932.
- [21] W.K. Liu, S. Li and T. Belytschko, Moving least square Reproducing Kernel Method (I) methodology and convergence, *Comput. Methods Appl. Mech. Engrg.* (1995), submitted.
- [22] W.K. Liu, Y. Chen, C.T. Chang and T. Belytschko, Advances in multiple scale Kernel Particle Methods, *Comput. Mech.* 18(2) (1996) 73–111.
- [23] W.K. Liu, Y. Chen, S. Jun, J.S. Chen, T. Belytschko, C. Pan, R.A. Uras and C.T. Chang, Overview and applications of the Reproducing Kernel Particle Methods, *Archives Comput. Methods Engrg. State of the Art Rev.* 3 (1996) 3–80.
- [24] J.S. Chen, C. Pan and C.T. Wu, Reproducing Kernel Particle Methods for rubber hyperelasticity, *Comput. Mech.*, in press.
- [25] P. Lancaster and K. Salkauskas, Surfaces generated by moving least squares methods, *Math. Comput.* 37 (1981) 141–158.
- [26] W.K. Liu, T. Belytschko and J.S. Chen, Nonlinear versions of flexurally superconvergent elements, *Comput. Methods Appl. Mech. Engrg.* 71(3) (1988) 241–258.

- [27] J.S. Chen, C.T. Wu and C. Pan, A pressure projection method for nearly incompressible rubber hyperelasticity, Part I: Theory, Part II: Applications, *ASME J. Appl. Mech.* (1995), in press.
- [28] A.N. Gent and E.A. Meinecke, Compression, bending and shear of bonded rubber blocks, *Polymer Engrg. Sci.* 10 (1970) 48–53.
- [29] N.T. Tseng, K. Satyamurthy and J.P. Chang, Nonlinear finite element analysis of rubber based products, The 131st Meeting of the Rubber Division, American Chemical Society, Montreal, Quebec, Canada, May 26–29, 1987.
- [30] E. Hinton, T.K. Hellen and L.R.R. Lyons, On elasto-plastic benchmark philosophies, in: D.R.J. Owen, E. Hinton and E. Onate, eds., *Computational Plasticity: Models, Software and Applications* (Pineridge Press, Swansea, UK, 1989) 389–408.
- [31] G.I. Taylor, The use of flat-ended projectiles for determining dynamic yield stress, Part I, *Proc. R. Soc. London, Ser. A* 194 (1948) 289–299.
- [32] M.L. Wilkins and M.W. Guinan, Impact of cylinders on rigid boundary, *J. Appl. Phys.* 44 (1973) 1200–1206.
- [33] W.W. Predebon, C.E. Anderson and J.D. Walker, Inclusion of evolutionary damage measures in Eulerian wavecodes, *Comput. Mech.* 7 (1991) 221–236.
- [34] D. Sulsky, S.-J. Zhou and H.L. Schreyer, Application of a particle-in-cell method to solid mechanics, *Comput. Phys. Comm.* (1995), submitted.
- [35] D.M. Norris, B. Moran, Jr., J.K. Scudder and D.F. Quinones, A computer simulation of the tension test, *J. Mech. Phys. Solids* 26 (1978) 1–19.
- [36] T.Y.P. Chang, A.F. Saleeb and G. Li, Large strain analysis of rubber-like materials based on a perturbed Lagrangian variational principle, *Comput. Mech.* 8 (1991) 221–233.
- [37] R.W. Penn, Volume changes accompanying the extension of rubber, *Trans. Soc. Rheol.* 14(4) (1970) 509–517.
- [38] T.J.R. Hughes and J. Winget, Finite rotation effects in numerical integration of rate constitutive equations arising in large-deformation analysis, *Int. J. Numer. Methods Engrg.* 15(12) (1980) 1862–1867.
- [39] R.D. Krieg and S.W. Key, Implementation of a time independent plasticity theory into structural computer programs, in: *Constitutive Evaluation in Viscoplasticity: Computational and Engineering Aspects*, AMD-29 (ASME, New York, 1976) 125–137.
- [40] J.C. Simo and R.L. Taylor, Consistent tangent operators for rate-independent elastoplasticity, *Comput. Methods Appl. Mech. Engrg.* 48 (1985) 101–118.